ARMY RESEARCH LABORATORY

Smoothed Particle Hydrodynamics Simulation of Disk-Shaped Penetrator Impact

Stephen J. Schraml
Kent D. Kimsey

ARL-TR-1766 AUGUST 1998

19981006 115

DTIC QUALITY INSPECTED 4

Approved for public release; distribution is unlimited.

The findings in this report are not to be construed as an official Department of the Army position unless so designated by other authorized documents.

Citation of manufacturer's or trade names does not constitute an official endorsement or approval of the use thereof.

Destroy this report when it is no longer needed. Do not return it to the originator.

Army Research Laboratory
Aberdeen Proving Ground, MD 21005-5066

ARL-TR-1766 August 1998

Smoothed Particle Hydrodynamics Simulation of Disk-Shaped Penetrator Impact

Stephen J. Schraml
Kent D. Kimsey
Weapons & Materials Research Directorate

Approved for public release; distribution is unlimited.

Abstract

Smoothed particle hydrodynamics (SPH) is a method of continuum mechanics analysis in which materials are modeled by a discrete set of particles. The SPH code Magi has been used to simulate the penetration of a semi-infinite steel target by tungsten alloy disks traveling at an initial impact velocity of 2 km/s. Calculations were performed to simulate experimental configurations using one, two, and four disks. All disks had a constant length-to-diameter ratio of 0.125. The computed penetration depth into the target material is compared to the experimental data for each case. The study included a set of calculations in which the problem resolution was varied to determine the ability of the method to converge on a penetration depth as the number of particles in the problem was increased. Advantages and limitations observed in the application of SPH to the field of penetration mechanics are discussed.

ACKNOWLEDGMENTS

The SPH code Magi discussed in this report is being developed by Larry Libersky of the New Mexico Institute for Mining and Technology. The initial installation of the code on a U.S. Army Research Laboratory (ARL) departmental computer system was performed with the valuable help of Ted Carney, also of New Mexico Tech. All the calculations described in this report were performed on the Silicon Graphics Origin 2000 computer systems located at the ARL Major Shared Resource Center. The photographs of the recovered penetrator from the impact experiments were taken by Lori Pridgeon of ARL. Valuable feedback about the technical content of this report was provided by Dixie Hisley of ARL and Phil Randles of the Defense Special Weapons Agency. The authors appreciate the support provided by these individuals and their respective organizations.

INTENTIONALLY LEFT BLANK

TABLE OF CONTENTS

		Page
	LIST OF FIGURES	vii
	LIST OF TABLES	ix
1.	INTRODUCTION	1
2.	SMOOTHED PARTICLE HYDRODYNAMICS	2
3.	SEGMENTED PENETRATOR EXPERIMENTS	5
4.	TWO-DIMENSIONAL AXISYMMETRIC SIMULATIONS	5
4.1.	Single-Disk Simulations	7
4.2.	Multiple-Disk Simulations	11
5.	THREE-DIMENSIONAL, SINGLE DISK SIMULATIONS	20
6.	INTERACTION OF REGIONS OF DIFFERENT PARTICLE SIZES	22
7.	VARIATION OF SMOOTHING LENGTH RETAINING CONSTANT PARTICLE SIZE	23
8.	SUMMARY AND RECOMMENDATIONS	26
	REFERENCES	29
	DISTRIBUTION LIST	33
	REPORT DOCUMENTATION PAGE	37

INTENTIONALLY LEFT BLANK

LIST OF FIGURES

Figure		Page
1.	The interpolation smoothing function	4
2.	Schematic diagram of disk impact test configuration	6
3.	Single-disk impact at 4 μs, 16 μs, 27 μs, and 100 μs (h=0.0635 cm)	9
4.	Tracer position history for single-disk impact (h=0.0635 cm)	10
5.	Tracer velocity history of single-disk impact (h=0.0635 cm)	10
6.	Predicted penetration channel for single-disk impact, particle size of: (a.) 0.0635 cm, (b.) 0.03175 cm, (c.) 0.02117 cm, and (d.) 0.015875 cm	12
7.	Single-disk penetration depth as a function of particle size	13
8.	Two-disk impact at 32 μs, 35 μs, 42 μs, and 100 μs (h=0.03175 cm)	15
9.	Pressure at center of leading face of second disk	16
10.	Recovered projectile from two-disk experiment	17
11.	Four-disk impact at 45 μs, 63 μs, 93 μs, and 150 μs (h=0.03175 cm)	18
12.	Tracer position history of four-disk impact (h=0.03175 cm)	19
13.	Target particle size variation for 3D model	21
14.	Single-disk penetration depth as a function of particle size (2D and 3D results)	22
15.	Single-disk impact at 40 μs for particle size ratios of: (a.) 0.50, (b.) 1.00, (c.) 1.30, and (d.) 2.00	24
16.	Penetration Histories from Smoothing Length Variation Study	26

INTENTIONALLY LEFT BLANK

LIST OF TABLES

Table		Page
1.	Material Properties	7
2.	Calculation Characteristics	13
3.	Smoothing Lengths used in 3D Target Models	20
4.	Calculations in Smoothing Length Variation Study	25

INTENTIONALLY LEFT BLANK

1. INTRODUCTION

Penetration and perforation of solids have long been of interest to the military. The development of armors to improve the survivability of military vehicles, the design of advanced penetrators and warheads to increase the lethality of weapon systems, and the application of blast and fragmentation mitigation devices to vehicles and buildings are fields of study requiring knowledge of penetration mechanics. The safety of nuclear reactor containment vessels, the development of lightweight body armors for police forces, the protection of spacecraft from meteoroid impact, and anti-terrorist technology are but a few non-military applications of the study of penetration phenomena. A thorough review of the fundamentals of penetration and perforation of solids and their application to practical problems has been prepared by Goldsmith (1960), Johnson (1972), Backman and Goldsmith (1978), and Zukas et al. (1982, 1990).

Impact and penetration events typically involve the interaction of various types of materials, the propagation of strong shock waves, large deformations and fracture of solid materials, high velocities, large strain rates, and detonation of explosives. Numerical methods in continuum mechanics have been used to model penetration phenomena since the 1950s. Early applications lacked the ability to model the strength characteristics of solids and considered only the *hydrodynamic* (i.e., density dominated) phenomena. Material strength and fracture criteria were implemented in these "hydrocodes" during the 1970s. However, the development of advanced material models is still an active area of research today, with particular emphasis on material damage, in-homogeneous materials, ceramics, and non-isotropic materials. A concise review of material behavior at high strain rates has been edited by Blazynski (1987).

Most numerical methods for continuum mechanics analysis involve the use of a grid or mesh to discretize the computational field (also referred to as the computational domain). For each cell or element within the computational field, the conservation equations are applied on a control volume basis. The global partial differential equations representing the conservation variables are transformed into algebraic equations that are applied locally at each cell. Numerical methods of this type fall into two categories: Eulerian and Lagrangian. In the Eulerian formulation, the conservation equations are applied from the perspective of events taking place at a fixed point in space. This formulation leads to a computational method in which the grid is fixed, and material motion is accomplished through transport of the material across the boundaries of cells within the grid. In the Lagrangian formulation, the conservation equations are derived on the basis of an observer that moves with the material. Consequently, in Lagrangian methods, the grid moves with the material and there is no transport of material across cell or element boundaries. Previous reviews of one-dimensional (1D) and two-dimensional (2D) codes for wave propagation and impact have been prepared by Mescall (1974), Von Rieseman et al. (1974), Herrman (1975), and Belytschko (1975). A review of three-dimensional (3D) wave propagation codes for impact problems is given by Zukas et al. (1982, 1990). Benson (1992) recently documented a comprehsive review of the physics and numerical methods for modeling the dynamics of impacting solids.

Each of these two approaches has a unique set of strengths and weaknesses when applied to the study of impact, shock wave propagation, large deformations, and material fracture. In Lagrangian methods, the material interfaces are defined by the shape of the mesh. Material interfaces, by definition, occur naturally along cell interfaces. Because the mesh moves with the material, time-dependent effects on the material are properly captured. However, for 3D cases involving complex geometries, grid generation can be a time-consuming task. Where large material deformations occur, Lagrangian methods can experience regions where the mesh is highly distorted, which can result in numerical instabilities and a very small time step. In regions where fracture is involved, it may be necessary for Lagrangian methods to automatically redefine the mesh to capture dislocations and spallation of material.

In Eulerian methods, relatively simple structured grids are typically employed and the material geometries are defined by the insertion of material into the grid. As a result, grid generation for Eulerian methods can be a trivial task. Because the grid is fixed, Eulerian methods are not prone to mesh distortions in cases involving large deformations. Material motion by transport across cell boundaries allows for fracture and spallation without the need for redefinition of the grid. The primary disadvantage of Eulerian methods lies in their inability to track material interfaces. Regions of the grid where different materials are in contact typically result in computational cells containing multiple materials and possibly some void. Material failure is typically handled by the insertion of void into cells that meet some material failure criteria. Computation of a thermodynamic state and application of material models for such mixed cells usually involves iterative computations weighted by the relative masses or volumes of the materials in the cell. Material interfaces in such cases must be generated artificially based on an interface tracking method. Material transport across cell boundaries may also result in loss of time-dependent effects in material characteristics.

These weaknesses of grid-based Euler and Lagrange methods provide sufficient motivation to study the application of alternate methods for modeling penetration mechanics problems. This report documents the application of the smoothed particle hydrodynamics (SPH) method for simulating high velocity impact experiments performed at the U.S. Army Research Laboratory (ARL).

2. SMOOTHED PARTICLE HYDRODYNAMICS

SPH is a meshless Lagrangian particle method that uses interpolation theory to establish estimates of field variables at a point. The Lagrangian formulation results in an accurate representation of material shapes and interfaces. The absence of an underlying mesh eliminates the possibility of time step instabilities that result from severe mesh distortion. Unlike Eulerian methods that require grid in regions of interest that may not contain any material, SPH employs particles only where material exists, resulting in a natural treatment of voids.

The SPH code that forms the basis of the current study, Magi, (Libersky et al., 1993; Randles & Libersky, 1996) employs an explicit time-marching algorithm to advance the solution from time t to time $t + \delta t$. Particle properties of density, velocity, energy, deviatoric

stress, and position are computed for time $t + \delta t$, based on values at time t according to Equations 1 through 5, respectively.

$$\rho^{n+1} = \rho^n \left(1 - D\delta t^n\right) \tag{1}$$

$$U_\alpha^{n+1/2} = U_\alpha^{n-1/2} + \frac{1}{2}\left(\delta t^n + \delta t^{n-1}\right) F \tag{2}$$

$$E^{n+1} = E^n + \delta t^n G \tag{3}$$

$$S_{\alpha\beta}^{n+1} = S_{\alpha\beta}^n + \delta t^n H \tag{4}$$

$$x_\alpha^{n+1} = x_\alpha^n + U_\alpha^{n+1/2}\delta t^n \tag{5}$$

In these equations, the $n+1$ superscript represents the solution at the new time, $t + \delta t^n$, while the n superscript identifies data from the time of the previous integration cycle, t. The time step identified by δt^n represents the time step that is used to advance the solution to the new time, while δt^{n-1} identifies the time step used in the previous integration cycle. The time step is computed by finding the minimum $wh/(c+s)$ over all particles, in which c is the sound speed, s is the particle velocity, h is the smoothing length used in the interpolation functions, and w is a constant stability factor between 0 and 1 (a value of 0.3 is typical). The subscripts α and β in Equations 1 through 5 denote spatial directions and are used individually as vector notation for positions and velocities and together to identify stress tensors.

The variables D, F, G, and H represent the volumetric strain, total acceleration, work per unit mass, and stress rate on a particle, respectively. These values are computed from the interpolation function, resulting in "kernel estimates" of field variables at a point. To compute the new values of the field variables for a particle, that particle's previous values and the values of its neighboring particles are used with the B-spline smoothing function shown in Equation 6:

$$W = \begin{cases} \frac{15}{7}\left(\frac{2}{3} - \nu^2 + \frac{1}{2}\nu^3\right) & 0 < \nu < 1 \\ \frac{5}{14}\left(2 - \nu\right)^3 & 1 < \nu < 2 \\ 0 & \nu > 2 \end{cases} \tag{6}$$

in which $\nu = |\mathbf{x}_i - \mathbf{x}_j|/h$. This smoothing function generates a weighting factor for the values of neighboring particles, which is based on the smoothing length, h, and the absolute distance of the neighboring particle from the particle of interest, $|\mathbf{x}_i - \mathbf{x}_j|$. This interpolation function is always positive, maximum at a distance of zero, and reaches zero at a distance of $2h$. Thus, to compute the new interpolation functions for a particle, the only neighboring particles that have an influence are those within a distance of two smoothing lengths of the

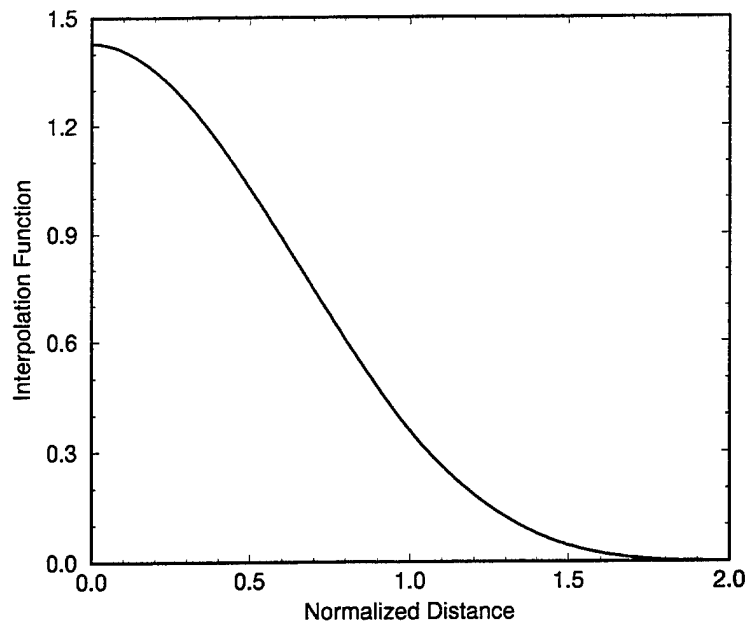

Figure 1. The interpolation smoothing function.

particle of interest. Figure 1 shows a plot of the B-spline as a function of relative distance from the particle of interest.

Because SPH is a meshless method, there is no underlying connectivity logic for particle interactions for a particular computation. The set of particles whose values must be used to compute the new state variables for a given particle depends on the positions of the particles. Because the particle positions are updated at every time step, a list of neighboring particles must be generated for each particle for every integration cycle. The set of neighboring particles that may interact with a given particle is defined by the smoothing function. Because the smoothing function depends on the smoothing length, h, a small smoothing length will result in fewer particles in the neighbor lists (and vice versa).

Thus, for every iteration in time, each particle must compare its position to all other particles in the computation and must build a neighbor list before the state variables can be updated. For a calculation containing N particles, this implies a workload of N^2 position comparisons for every iteration in time. To decrease the workload associated with finding neighbors, an artificial, rectilinear grid is generated over the computational space. Particles are then assigned to the cells of this artificial grid. The cells within the artificial grid have sides of length $2h$, the range of the smoothing function. As previously stated, the time-marching scheme is explicit. Thus, for a particular time step, a particle may only interact with, at most, the other particles in its artificial cell and those in the immediate neighbor cells. This approach reduces the workload of constructing neighbor lists from N^2 to approximately $Nlog(N)$.

3. SEGMENTED PENETRATOR EXPERIMENTS

The penetration performance of high density, low length-to-diameter (L/D) ratio projectiles impacting steel targets has been a topic of considerable interest in penetration mechanics because of the speculated performance of a segmented rod projectile. This has been spurred by the observation that relative projectile performance, i.e., penetration per unit length (P/L), increases as L/D decreases, provided that the impact velocity is relatively high. Computational and experimental research to date has focused on penetrators shaped as either right-circular cylinders with an L/D of one or slightly greater, or spheres (Brissenden, 1992; Charters et al., 1990; Charters, 1987; Charters & Orphal, 1990; Cline et al., 1989; Cuadros, 1990; Frank & Zook, 1990; Hauver & Melani, 1990; Hohler & Stilp, 1990; Holland et al. 1990; Hunkler, 1989; Kivity et al. 1989; Naz & Lehr, 1990; Raatschen et al., 1989; Scheffler & Zukas, 1990; Scheffler, 1990; Sorensen et al., 1991; Tate, 1990; Zukas, 1990). De Rosset and Sherrick (1996) modeled segmented rod performance at ordnance velocity for high density tungsten alloy segments with an L/D of one. They observed that multiple-segment rod performance was less than that predicted by simply multiplying single segment performance by the total number of segments, because of interactions with residual segment material in the penetration cavity.

Recently, computational and experimental studies have focused on characterization and understanding of the penetration mechanics of high density metallic projectiles with an L/D of less than one (Bjerke et al., 1992; Orphal et al., 1990; Orphal et al., 1992). Herbette (1989) noted a dramatic increase in P/L for steel disks with an L/D ratio of 1/30 impacting aluminum targets at 2 km/s, when compared to penetrators with considerably greater L/D. Orphal and Fransen (1990) also reported a significant increase in P/L as projectile L/D was reduced from 1 to 1/8 for tungsten, tungsten alloy, and tantalum alloy projectiles impacting steel targets at striking velocities between 1.5 km/s and 7.5 km/s.

Experiments have been conducted at ARL in which tungsten alloy disk penetrators were launched into semi-infinite rolled homogeneous armor (RHA) steel targets at a striking velocity of 2.0 km/s (Bjerke, 1997). The disks were 1.27 cm in diameter and had a thickness of 0.3175 cm (L/D = 1/8). Experiments were performed using one, two, and four disks. For the cases using more than one disk, the spacing between adjacent disk faces was 5.08 cm (two disk diameters). The experiments were designed to have all the disks aligned axially with the faces of the disks parallel to the face of the target material on impact. A schematic diagram of the experimental configuration is provided in Figure 2.

4. TWO-DIMENSIONAL AXISYMMETRIC SIMULATIONS

A series of calculations was performed in a 2D axisymmetric geometry to simulate the experiments conducted by Bjerke. The simulation of the tests in an axisymmetric geometry is reasonable as the tests resulted in nearly perfect axial alignment of the disks and normal impact of the disks with the target. The semi-infinite RHA target material was modeled as a continuous set of particles with a radius of 10 cm and a depth of 10 cm. Transmissive

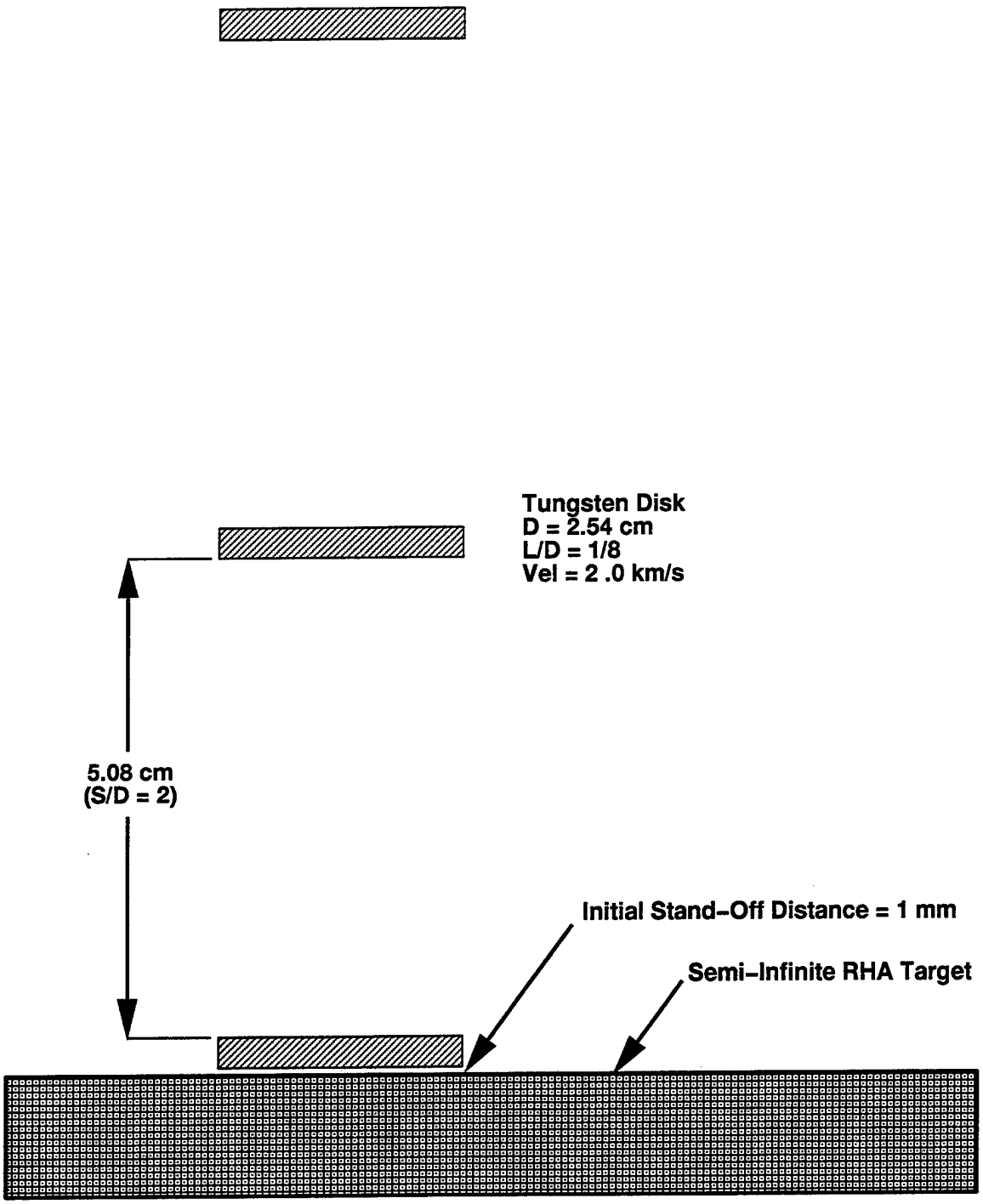

Figure 2. Schematic diagram of disk impact test configuration.

boundaries were placed at the outer radius of the target and at the bottom of the target (opposite the point of impact) to model the semi-infinite nature of the target. The hydrodynamic behavior of the tungsten alloy disks and the RHA target materials was modeled with a linear Hugoniot shock-particle velocity equation of state. An elastic/perfectly plastic plasticity model was used for all materials. A summary of the material properties is provided in Table 1.

Table 1. Material Properties.

	Tungsten	RHA
Density (g/cm^3)	17.270	7.842
Sound Speed (m/s)	4237	4529
Slope of U_s-U_p	1.24	1.50
Grüneisen Parameter	1.80	1.84
Specific Heat at Constant Volume (cal/g-K)	0.036	0.107
Yield Strength (kbar)	19.3	7.0
Shear Modulus (Mbar)	1.606	0.816
Fracture Pressure (kbar)	-30.0	-25.0

4.1. Single-Disk Simulations

The first SPH calculation in the study simulated the impact of a single disk. This calculation employed a smoothing length, h, of 0.0635 cm, with one particle per smoothing length. This resulted in a distribution of five particles across the thickness of the disk and 20 particles across the radius, for a total of 100 particles in the disk. The target was modeled with the same smoothing length characteristics and consequently had identical particle sizes as the disk. In all, the target contained 24,649 particles. As shown in Figure 2, the disk was initially positioned above the target with its impact face positioned 1 mm from the impact face of the target. The calculation was run to a simulated time of 100 μs, requiring 2,527 time iterations.

When the disk strikes the target, one compression wave is established in the target and another is established in the disk. Because the disk is very thin (0.3175 cm), the initial compression wave propagating through it reaches the back face of the disk at approximately 0.75 μs, at which time, it reflects back toward the impact face of the disk in the form of an expansion wave. This expansion wave propagation causes the disk material to decelerate, resulting in the formation of a void region between the disk and the target at the centerline of the impact. This void grows and then ultimately collapses, resulting in renewed contact between the disk and target material at the centerline as the penetration process continues.

This process is illustrated in Figure 3 which provides a set of material plots at times of 4 μs, 16 μs, 27 μs, and 100 μs during the simulation. Since the simulation was performed using symmetry about the y-axis, the materials in these plots have been reflected about the y-axis to show the actual physical geometry. While the target material was modeled having a radius of 10 cm, the plots are limited to a radius of 3 cm. The plot at 4 μs shows the initial

penetration of the disk into the target material. The event at this time is characterized by the nearly horizontal material interface and the beginning of the formation of a void region at the disk-target interface. At 16 μs, this void region has grown to its maximum and then begins to collapse until the two materials are again in contact at the centerline at 27 μs. The material plot at 100 μs shows the final shape of the penetrator and the target. The predicted depth of penetration is 1.34 cm, for a P/L of 4.2. The predicted P/L is 12.4% lower than the experimental mean and is also in good agreement with previous computational values (Bjerke et al., 1992).

Two Lagrangian tracers were employed in this calculation to gather particle history data. One tracer was attached to the centerline particle on the impact face of the disk. The other tracer was placed in the target material, attached to the centerline particle at the impact face. Analysis of the position and velocity histories of these two particles reveals the growth and collapse of the void region between the two materials. Figure 4 provides the y-position (axial) histories of these two particles as well as a history of the distance between the two particles. Figure 5 provides the y-velocity (axial) histories of the tracers. The data provided by the tracers yield the center position of the particles. Because each particle has a finite radius equivalent to half the smoothing length, h, the minimum difference between two adjacent particles that are in contact is approximately h. This is illustrated in the position-difference curve in Figure 4. Initially, the disk tracer particle moves downward and as the impact process begins, the target tracer particle is accelerated. At approximately 2 μs, the distance between the two tracers is at a minimum.

After the initial contact between the disk and the target, propagation of the expansion wave through the disk, coupled with concentration of radial waves at the centerline, decelerates the disk particles near the centerline and causes the formation of the void region between the disk and the target. This void region grows to a maximum at 16 μs and then decreases until the two tracers are again in contact at 27 μs, as illustrated by the position-difference curve in Figure 4.

The velocity histories in Figure 5 show the initial velocity of the disk tracer as -2 km/s, the impact velocity of the disk. The velocity of the target tracer is initially zero and is accelerated until the two tracers have a common velocity of approximately -1.25 km/s at approximately 1 μs. The two tracers share a common velocity until approximately 2.5 μs, after which, the velocity of the target tracer is larger than that of the disk tracer, resulting in the formation of the void region. By 16 μs, the void has reached its maximum and is marked by the crossing of the two velocity histories. After this time, the void closes until the two tracer particles are again in contact and share a common velocity at 30 μs. By 38 μs, the maximum penetration depth has been achieved.

After this baseline single-disk simulation was completed, three additional calculations were performed to assess the ability of the code to converge on a solution with increasing resolution. As stated earlier, the baseline calculation employed a particle size of 0.0635 cm to produce five particles across the thickness of the disk. The next three single-disk cases employed particle sizes of 0.03175 cm, 0.02117 cm, and 0.015875 cm, which resulted in 10, 15, and 20 particles across the disk thickness, respectively. Each of these calculations was run

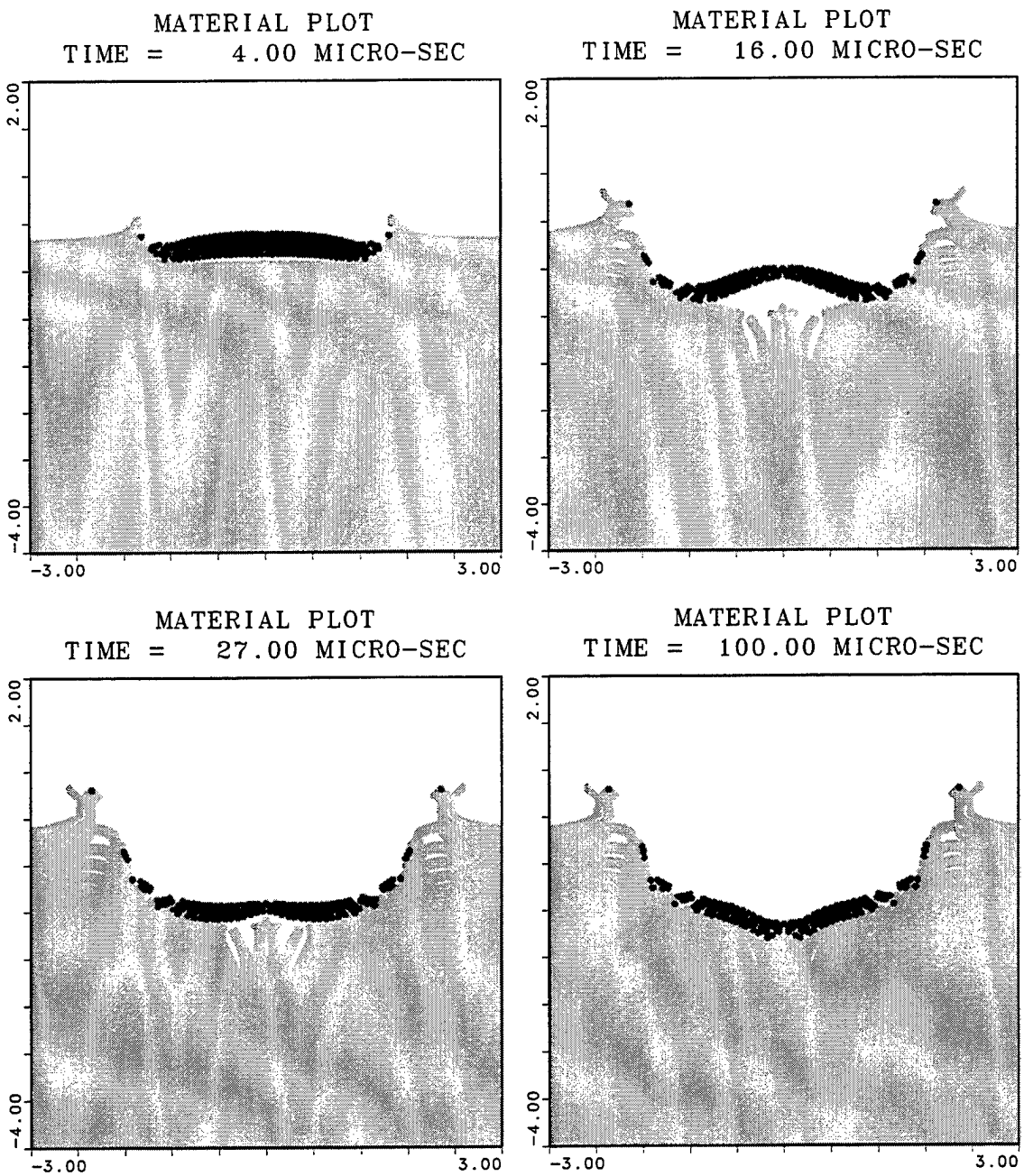

Figure 3. Single-disk impact at 4 μs, 16 μs, 27 μs, and 100 μs (h=0.0635 cm).

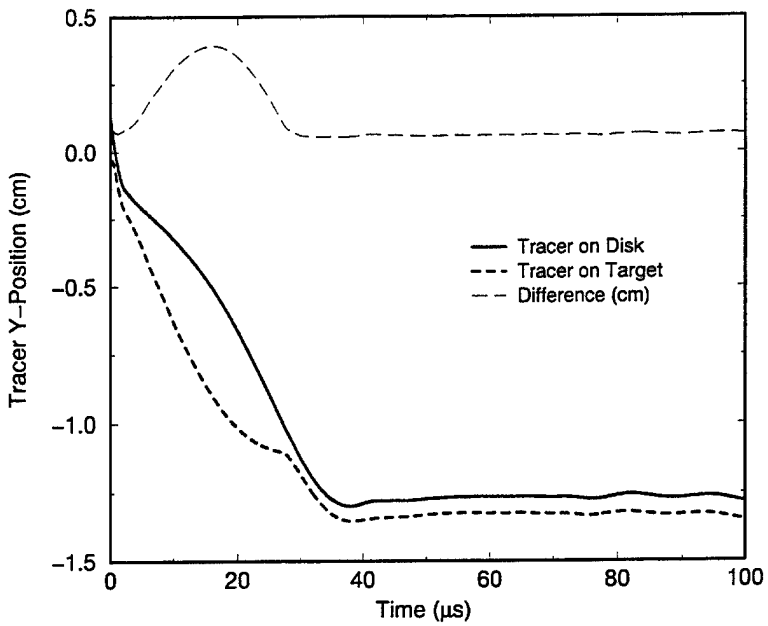

Figure 4. Tracer position history for single-disk impact (h=0.0635 cm).

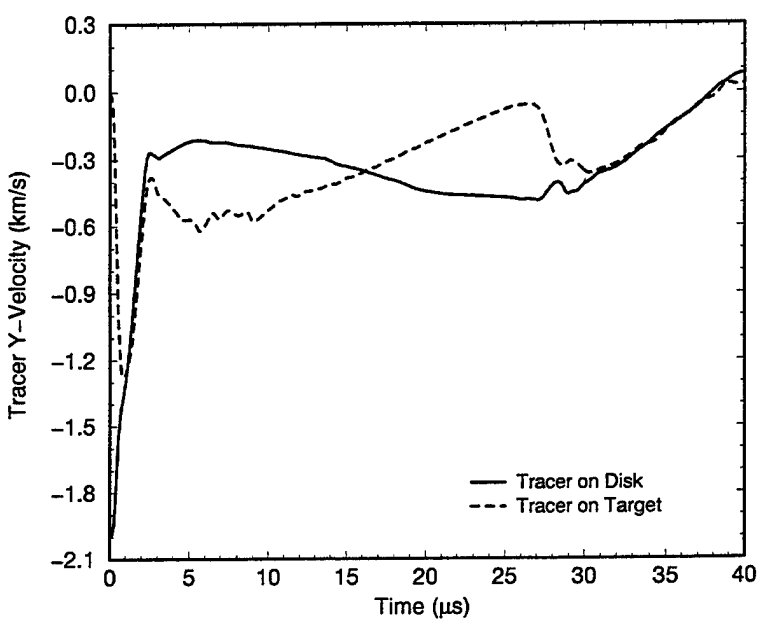

Figure 5. Tracer velocity history of single-disk impact (h=0.0635 cm).

for a simulated time of 100 μs. Material plots for each of the four calculations, showing the final penetration into the target, are provided in Figure 6. Each of these results shows the target to have a final crater shape that is approximately spherical, with a small additional depression near the centerline. These plots also show some erosion of the penetrator and a similar depressed region near the centerline.

The plot in Figure 7 shows the final penetration depth for each single-disk calculation as a function of the particle size. This figure shows that the penetration depth for the baseline case is much less than that for the higher resolution cases and that the penetration depth converges as the number of particles is increased. The case that employed five particles across the disk thickness produced a final penetration depth of 1.34 cm, while the cases using 10, 15, and 20 particles all produced penetration depths of 1.43 cm. These results indicate that the use of five particles to model a critical dimension (in this case, the disk thickness) is insufficient to properly capture the physics of the penetration event. Furthermore, the results show that there is no benefit in using more than 10 particles across the critical dimension for this problem.

Also included in Figure 7 is a data marker to represent the experimental data collected for the single-disk configuration (Bjerke et al., 1992). A total of four tests was performed, resulting in a mean penetration depth of 1.53 cm, with a sample standard deviation of 0.26 cm. The experimental data are represented in Figure 7 as a data point at the mean value with an error bar whose size is one standard deviation. The figure shows that the computational result using five particles across the disk thickness falls below the experimental data range, while the higher resolution calculations fall within the variation of the experimental data, with a final penetration depth that is 6.5% less than the experimental mean.

These findings are consistent with the general application of Eulerian methods to problems involving strong shock wave propagation. In these cases, it is considered good practice to employ at least five to ten Eulerian cells across the smallest critical dimension in a simulation. As in the use of Eulerian codes, the implementation of this practice in SPH is strictly dictated by the overall memory and processor limitations of the computer being used to run the simulation. Improved problem definition will dramatically increase the memory and run time requirements since the workload in a 2D simulation is proportional to $(1/h)^3$, while that of a 3D simulation is proportional to $(1/h)^4$. To illustrate this point, the number of particles, number of time integration cycles, and the computer time are summarized for each single-disk calculation in Table 2.

4.2. Multiple-Disk Simulations

Additional disk impact experiments were performed in which sets of two or four disks were launched into the semi-infinite RHA target material. For all of the multiple-disk tests, the spacing between adjacent disks was 5.08 cm (two disk diameters), as illustrated in Figure 2. Based on the information gained from the single disk simulations, the multiple-disk calculations used a smoothing length of 0.03175 cm, with one particle per smoothing length yielding ten particles across the thickness of each disk.

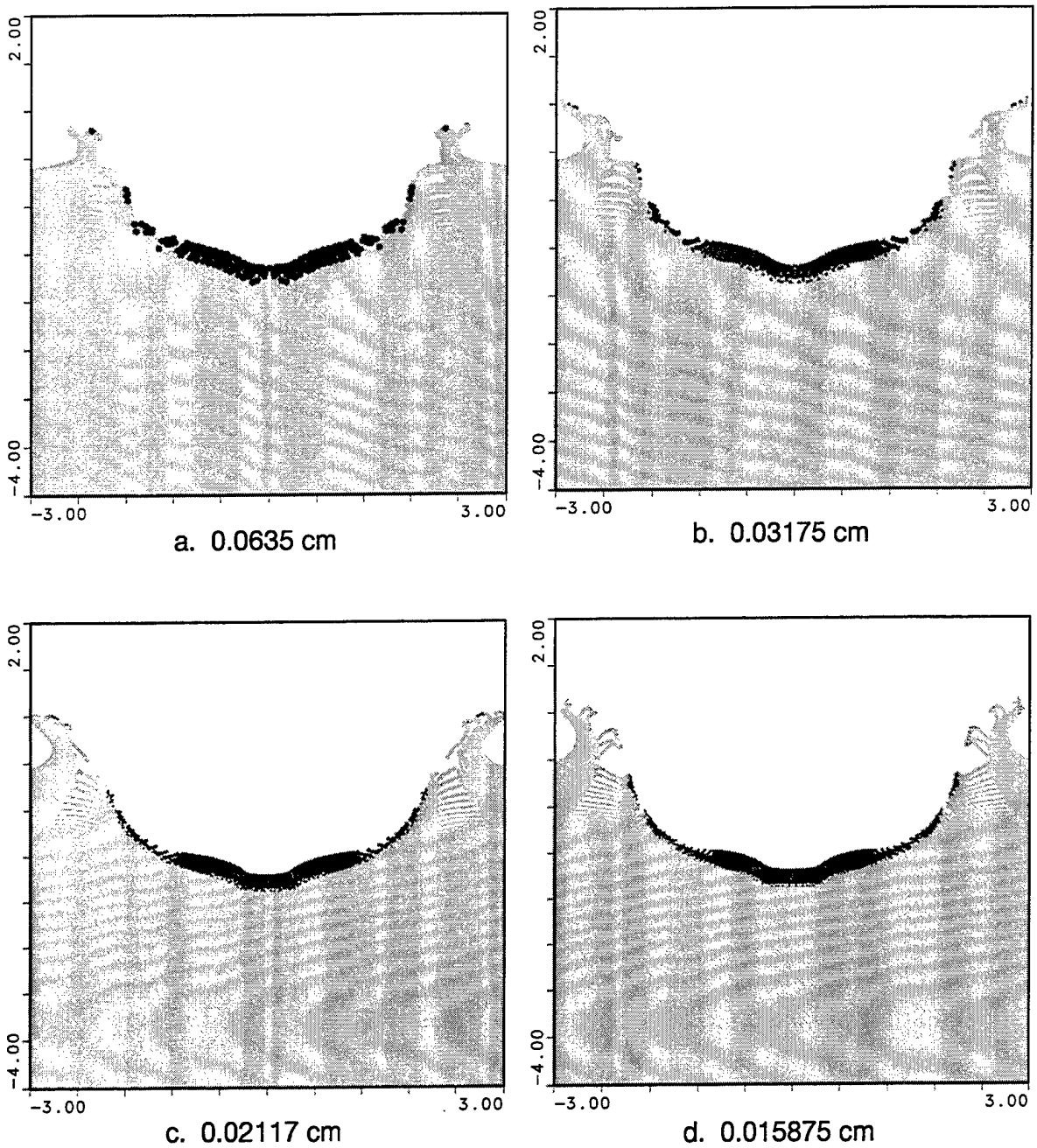

Figure 6. Predicted penetration channel for single-disk impact, particle size of: (a.) 0.0635 cm, (b.) 0.03175 cm, (c.) 0.02117 cm, and (d.) 0.015875 cm.

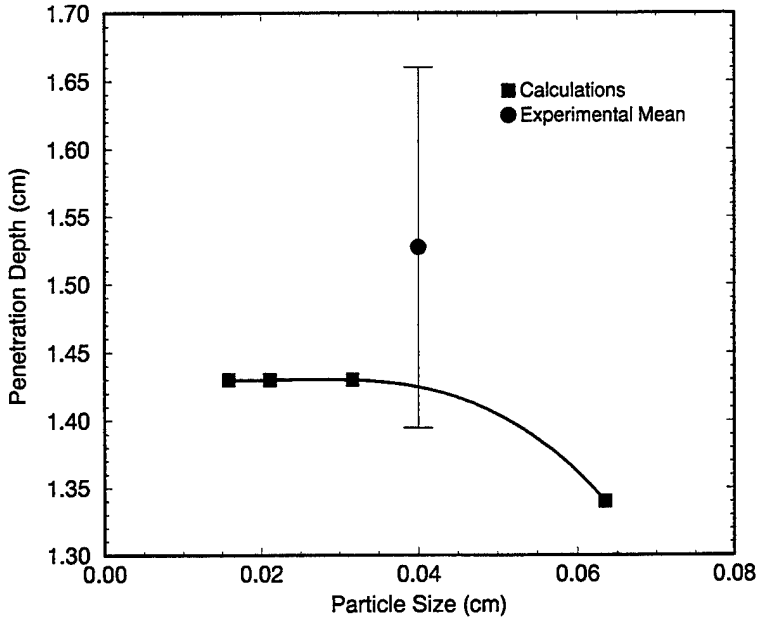

Figure 7. Single-disk penetration depth as a function of particle size.

Table 2. Calculation Characteristics.

	Particle Size (cm)			
	0.0635	0.03175	0.0217	0.015875
Particles Across Disk Thickness	5	10	15	20
Particles in Disk	100	400	900	1600
Particles in Target	24649	99225	222784	396900
Total Particles	24749	99625	223684	398500
Cycles‡	2527	5135	7766	10317
Penetration Depth (cm)	1.34	1.43	1.43	1.43
Computer Time† (hours)	1.0	8.2	27.3	66.5

‡ 100 μs simulated time
† 195 MHz Silicon Graphics R10000 processor

Figure 8 illustrates the penetration of the two disks into the target at simulated times of 32 μs, 35 μs, 42 μs, and 100 μs. At 32 μs, the initial contact between the two disks occurs at the outer radius of the second disk. Before this initial contact between the two disks, the calculation was identical to the single-disk case. This initial contact at the outer radius initiates a set of radially propagating compression waves that will ultimately converge at the centerline of the disk. By 35 μs, the face of the second disk at the centerline has contacted the first disk. The convergence of the radially propagating compression waves at the centerline of the disk, coupled with the waves generated by the impact of the face of the disk at the center, results in a strong expansion wave that is responsible for failure of the disk material near the center. The image in Figure 8 for 35 μs provides the initial indication of material failure as the particles near the center of the disk are beginning to diverge at this time, sending a jet of failed disk material in the opposite direction of the disk motion. At 42 μs, the void in the center of the disk has grown to its maximum size with the bulk of the disk material still carrying momentum in the direction of the target. By the end of the simulation at 100 μs, this momentum has caused the void at the center to partially close, with a small void remaining at the center.

To further illustrate the cause of failure of the second disk, the pressure obtained from the tracer at the center of the leading face of this disk is presented in Figure 9. This figure has two history plots. The upper plot shows the full 100-μs range of tracer data. At the time of impact of the second disk, the pressure reaches a peak of approximately 4 Mbar. The lower plot provides a magnified view of the data centered about the time of impact of the second disk. This plot shows that the initial pressure peak in the upper plot occurs at approximately 33 μs and has a duration of approximately 1 μs. After this positive pressure phase, the pressure becomes negative and quickly reaches the tensile limit of the tungsten alloy at -30 kbar. Because the material is not permitted to support tension beyond this threshold pressure, the curve is flat at -30 kbar until the particle again sees compression. A second negative phase occurs between 35 μs and 36 μs, which again exceeds the tensile limit of the disk material.

Of the set of two disk experiments that were conducted, only one had sufficiently low yaw angle of both disks and axial alignment of disks to qualify it as an axisymmetric event. For this experiment, the final penetration depth into the target material was 2.35 cm. The calculation produced a total penetration depth of 2.78 cm, which is approximately 18% greater than the experiment. Since there is only one experimental data point, it is impossible to determine the error in the experimental data for this two-disk configuration. However, one would expect the experimental scatter to be at least as large as that for the single-disk case.

The second disk was recovered from the experiment and a photograph of this disk is provided in Figure 10. The impact face of the disk is facing the camera and the photograph shows a hole in the disk as predicted by the calculation. One can see that the hole in the recovered disk is not exactly in the center of the disk and that the disk is not perfectly round. These characteristics are considered to be a result of small asymmetries in the experiment.

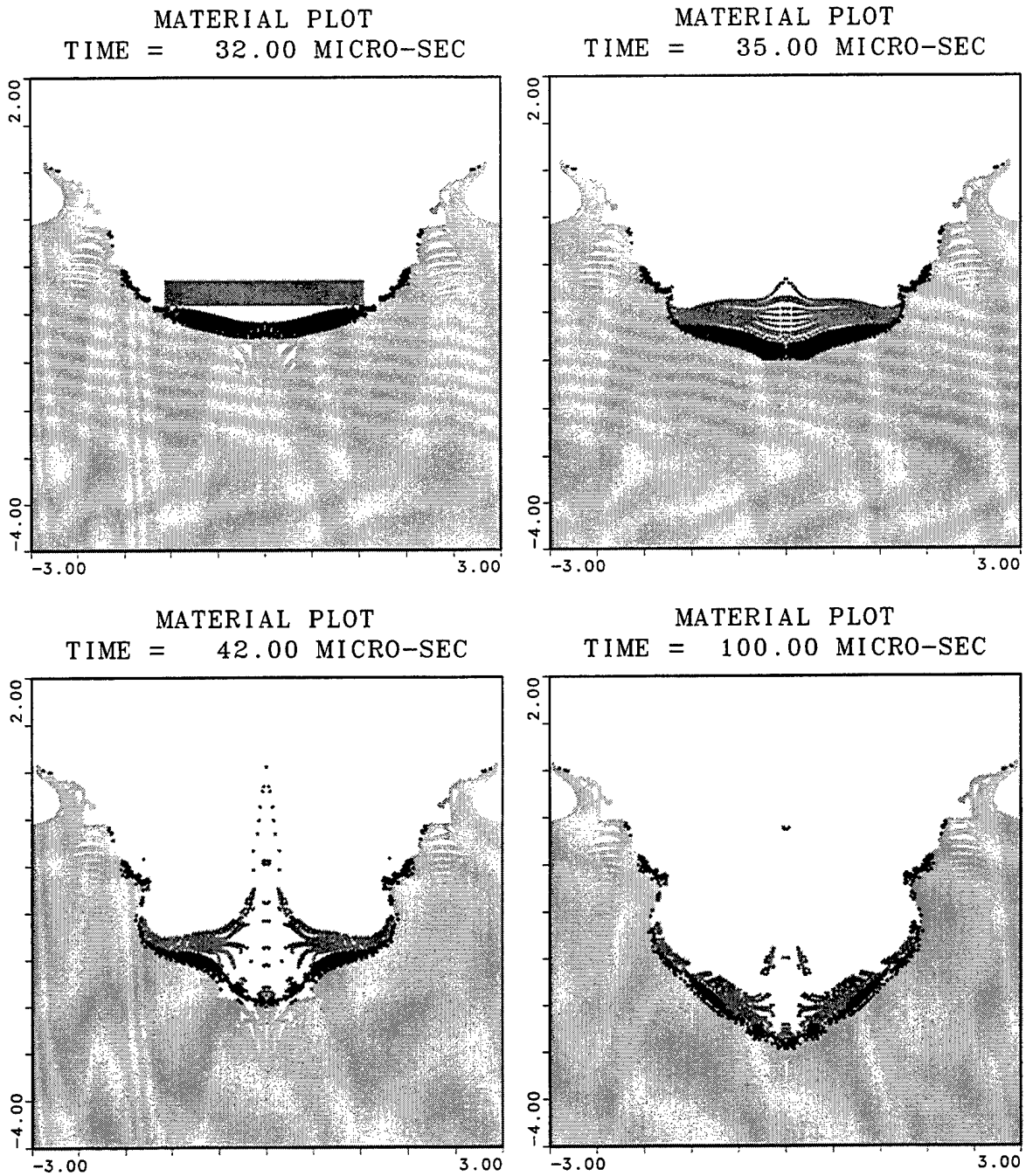

Figure 8. Two-disk impact at 32 μs, 35 μs, 42 μs, and 100 μs (h=0.03175 cm).

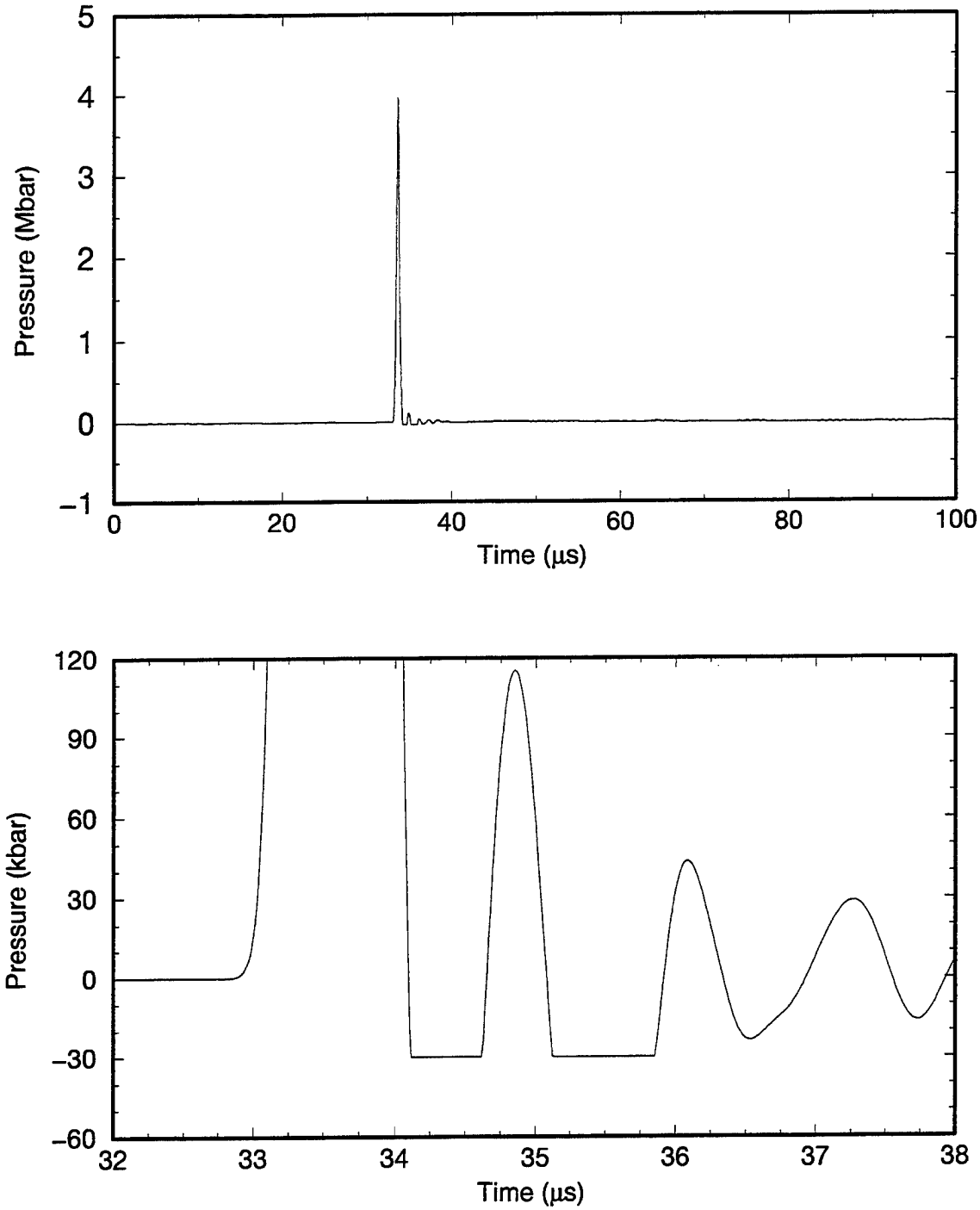

Figure 9. Pressure at center of leading face of second disk.

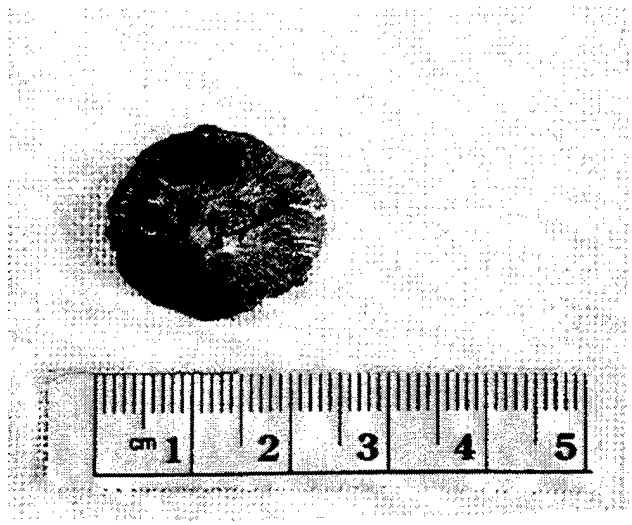

Figure 10. Recovered projectile from two-disk experiment.

The width of the recovered disk varies approximately from 2.0 cm (measured vertically on the photograph) to 2.3 cm (measured horizontally on the photograph). The final state of the calculation, as illustrated in the 100-μs frame of Figure 8, shows that the second disk has some eroded material deposited along the wall of the crater and the eroded material is separated from the main body of the disk. The main body has the void region at the center and a radius of approximately 2.4 cm, which compares well to the size of the recovered disk.

The final axisymmetric calculation run in this study was a simulation of a four-disk impact experiment. As in the two-disk case, the separation distance between adjacent disks was 5.08 cm, and the smoothing length was 0.03175 cm, with one particle per smoothing length. Lagrangian tracers were placed on the impact face of the target and on each face of the disks along the axis of symmetry. The calculation was run to a simulated time of 150 μs, and a solution image was saved at 1-μs intervals for the purpose of post-processing the results.

Figure 11 provides material plots to illustrate four of the most significant events in the simulation. In the two-disk case, it was shown that the second disk experienced failure at the center upon impact with the first disk. This failure sent a jet of disk material backwards, in the opposite direction of the disk motion. In the four-disk simulation, the third disk initially encounters this debris jet of material after 45 μs and is severely damaged by the debris jet before it begins to interact with the target at the bottom of the crater created by the first two disks.

The material plot at 63 μs shows a failed region in the center of the third disk as it makes initial contact with the material at the bottom of the crater. This damage decreases the ability of the third disk to penetrate the target. Some of the material that caused the failure of the third disk at the centerline, as well as some failed material from the third disk itself, continue to produce a debris jet that encounters the fourth disk as it approaches the bottom of the crater. The material plot at 93 μs shows slight damage to the fourth disk before impact on the crater. The large void region near the centerline left by the failure of

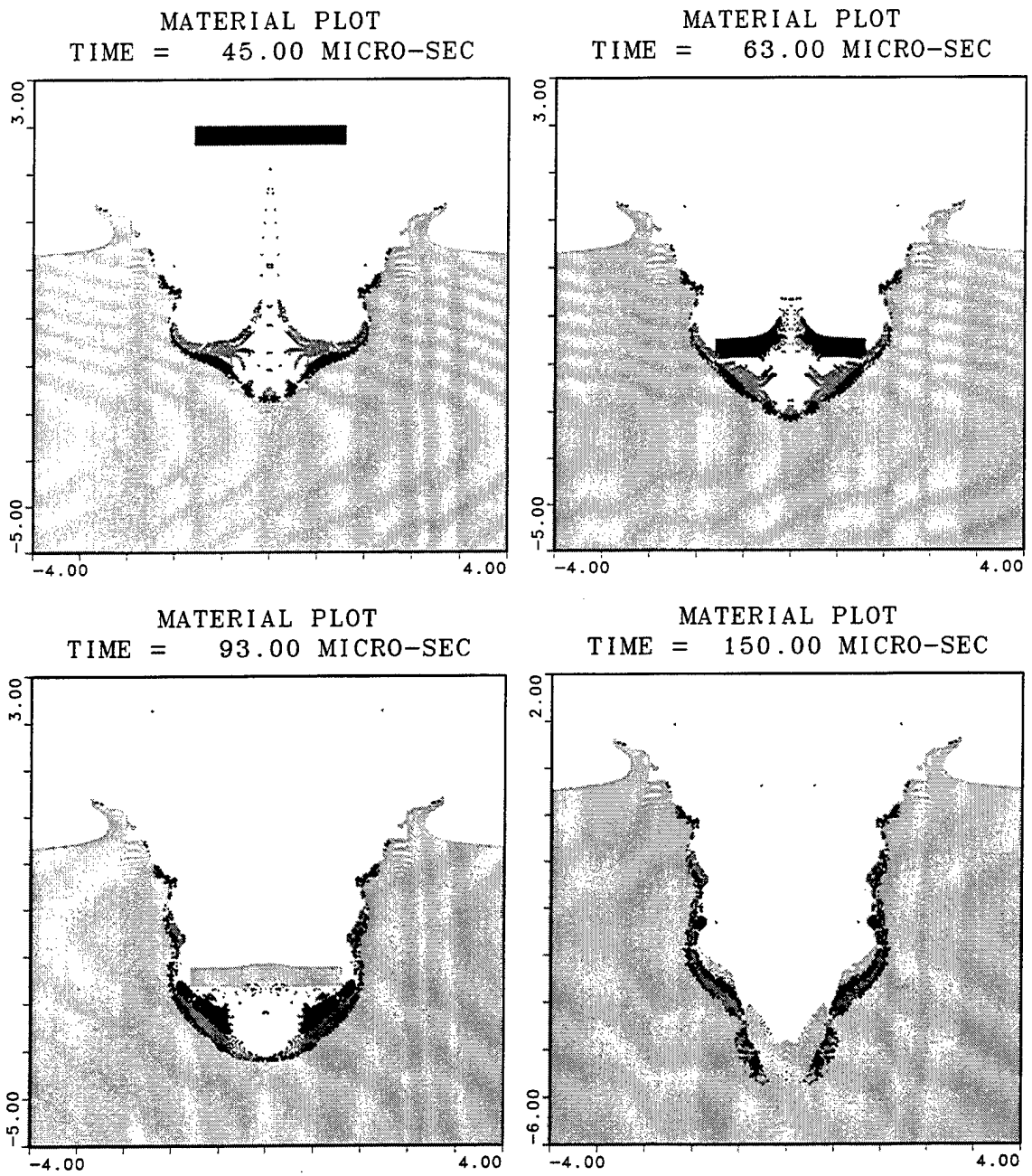

Figure 11. Four-disk impact at 45 μs, 63 μs, 93 μs, and 150 μs (h=0.03175 cm).

the third disk causes the fourth disk to fold upward near the outer radius, focusing the mass toward the centerline. The material plot at 150 μs in Figure 11 shows the final state of the calculation with most of the material of the first three disks deposited along the walls of the crater and most of the material from the fourth disk at the bottom of the crater in the center.

The position history of the Lagrangian tracer on the impact face of the target can be seen in Figure 12, which shows four distinct impacts by the individual disks. Immediately before the arrival of the second disk, the first disk had penetrated 1.40 cm into the target. When the third disk arrived, the penetration of the second disk was almost complete and had contributed an additional 1.41 cm. The same is true for the third disk; yet, it only contributes 0.79 cm to the overall penetration depth. Finally, the fourth disk adds another 1.36 cm, to bring the total penetration depth to 4.96 cm. Analysis of the data in Figure 12 shows that the first, second, and fourth disks provide almost equal contribution to the overall penetration, while contribution from the third disk was less than 60% of any of the other three. The performance degradation is a result of the interaction of the third disk with the failed material (i.e., debris jet) of the second disk and subsequent centerline failure.

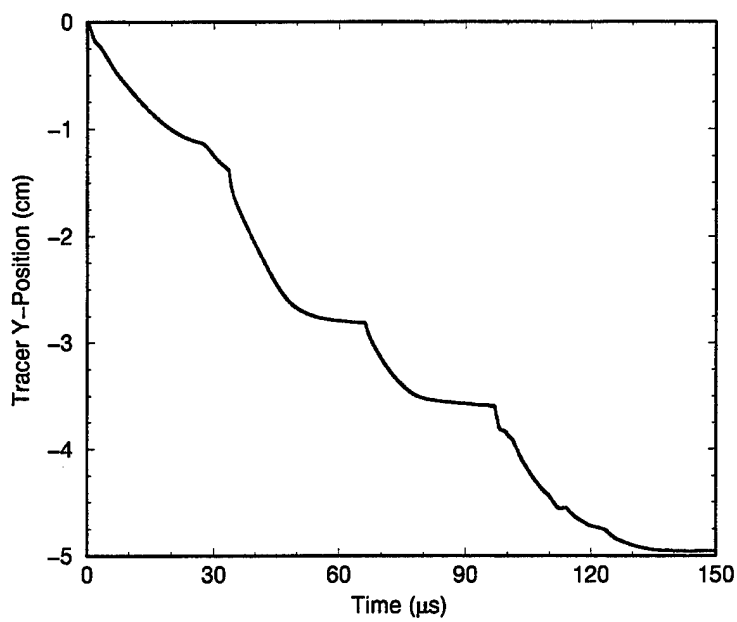

Figure 12. Tracer position history of four-disk impact (h=0.03175 cm).

Like the two-disk case, there exists only one experiment using four disks with disk alignment and yaw qualities that can be characterized as an axisymmetric configuration. For this experiment, the total penetration depth of the four disks into the semi-infinite RHA target was 4.45 cm, approximately 11.5% less than that predicted by the calculation. As with the two-disk experiment, the scatter in the experimental data for this test configuration is not known.

5. THREE-DIMENSIONAL, SINGLE DISK SIMULATIONS

To evaluate the capabilities of the 3D implementation of the SPH code, a set of calculations was performed to simulate the single-disk impact tests. As in the case of the axisymmetric calculations, a smoothing length resolution study was performed to assess the ability of the 3D code to converge on a final penetration depth as the problem resolution was improved. This study would have the benefits of allowing for a direct comparison between the results of geometrically identical 2D and 3D calculations. It would also reveal any additional modeling challenges that exist in 3D that may not be present in 2D and would provide data about the amount of computer resources (time, memory, disk storage) that would be required to perform a realistic simulation.

The primary difference between the 3D models used in this set of calculations and those used in the axisymmetric cases is the definition of particles in the target. The axiymmetric models that were used to simulate the single-disk experiments modeled the target as a solid block with a radius of 10 cm and a depth of 10 cm, with a set of uniformly sized particles distributed throughout the target. Similarly, the 3D model represented the target material as a solid block with a half width (distance from impact point to outer edge) of 12.7 cm and a depth of 12.7 cm (ten disk radii). However, the distribution of a uniform set of particles throughout this target would have resulted in an unacceptably large number of particles in the target, resulting in very large computational requirements.

To reduce the number of particles in the target, the 3D computational model was defined so that target particles identical in size to the particles in the penetrator were used in the region where the interaction between the two bodies was to occur. Successive layers of increasing particle size were then used to transition from this central region of interest to the boundaries of the computation. Figure 13 illustrates the particle size variation in the target for the 3D model.

In the figure, the target particles are shaded and sized according to the value of the smoothing length, h. Six regions of constant smoothing length are used to vary the particle size across the dimensions of the target. These regions are identified by the $\mathbf{h}_1$ through $\mathbf{h}_6$ labels in Figure 13. The ratio of particle sizes in two adjacent regions is 1.75. A listing of all the smoothing lengths used in the 3D calculations is provided in Table 3.

Table 3. Smoothing Lengths used in 3D Target Models.

Particles Across Disk Thickness	Smoothing Length (cm)						Total Particles in Model
	h_1	h_2	h_3	h_4	h_5	h_6	
5	0.06350	0.11113	0.19447	0.34032	0.59556	1.04223	187894
6	0.05292	0.09260	0.16206	0.28360	0.49630	0.86853	309554
7	0.04536	0.07938	0.13891	0.24309	0.42540	0.74445	488568
8	0.03969	0.06945	0.12154	0.21270	0.37223	0.65139	731090
9	0.03528	0.06174	0.10804	0.18907	0.33087	0.57902	1034672
10	0.03175	0.05556	0.09723	0.17016	0.29778	0.52112	1442442

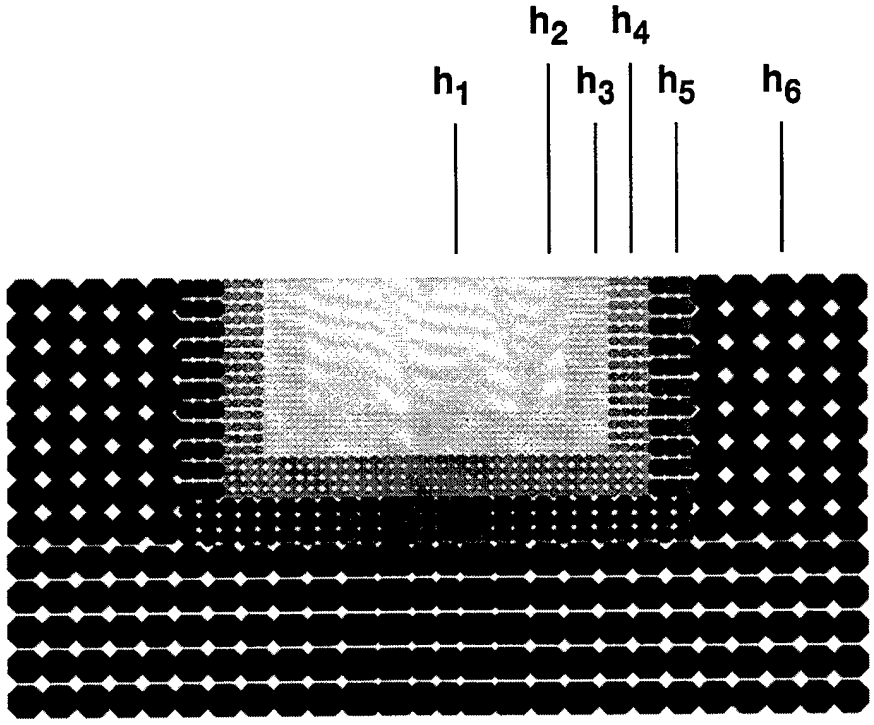

Figure 13. Target particle size variation for 3D model.

Calculations using the models described in Table 3 were run for a simulated time of 40 μs. This simulation time is based on the previous 2D single-disk impact simulations that showed the penetration event to be complete by 40 μs. Because the code employs an explicit solution method, the time required to complete a 3D simulation is proportional to the fourth power of the inverse of the particle size. Thus, reducing the particle size by a factor of two will increase the run time by a factor of 16. The same is true for explicit grid-based methods. In the case of the 3D calcualtions presented here, the case using a minimum particle size of 0.06350 cm completed in 11 hours. However, the calculation that used a minimum particle size of 0.03175 cm required 186 hours to complete. This is consistent with the fourth power estimate from the first calculation. The run times of the other calculations in the set were likewise consistent with the estimated times.

Figure 7 compares the penetration depths of the axisymmetric calculations to the experimental data. Figure 14 is a reproduction of that figure, with the addition of the penetration depths from the 3D calculations. As can be seen in the figure, the 3D calculations produce a different convergence behavior than the axisymmetric code. For all particle sizes, the final penetration depth of the 3D code is less than its axisymmetric equivalent. Like the axisymmetric calculations, the calculation using the largest particles produced the least penetration depth. The penetration depth increases with problem resolution up to a particle size of 0.03969 cm. This calculation is the only one in the set for which the final penetration depth falls within the range of uncertainty of the experimental data. For the two cases with smaller particles than this case, the final penetration depths were slightly lower. Additional calculations with even smaller particles may show whether or not true convergence

was obtained, but the run times of such cases would be prohibitively long. One possible explanation for the under-prediction of the penetration depth of the 3D code, as compared to the axisymmetric calculations, may be the variation of particle sizes in the target. The interaction of particles of different sizes is the subject of the next section of this report.

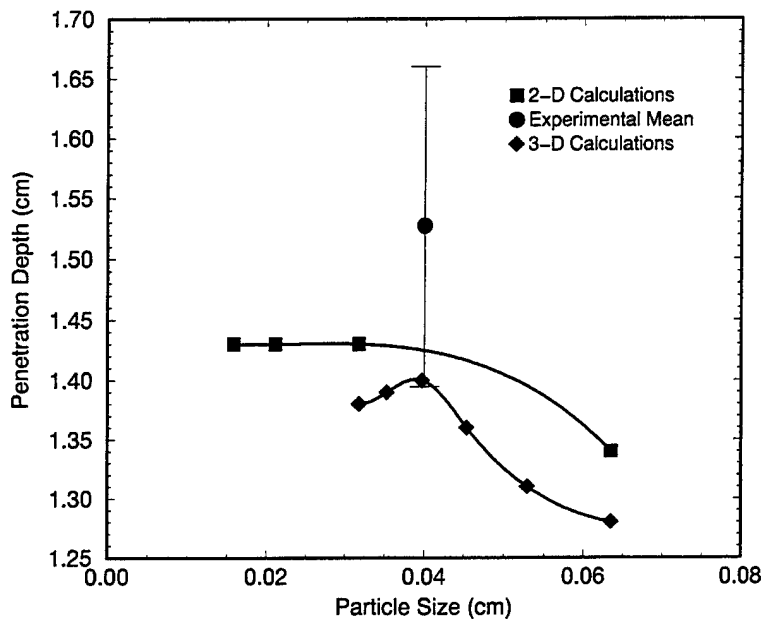

Figure 14. Single-disk penetration depth as a function of particle size (2D and 3D results).

6. INTERACTION OF REGIONS OF DIFFERENT PARTICLE SIZES

The 3D calculations described in the previous section had the target material modeled with multiple sets of particles, gradually increasing in size with increasing distance from the region of interest. As noted earlier, the ability of the 3D code to converge on a final penetration depth with increasing problem resolution differed significantly from the results of the axisymmetric simulations. One possible explanation for this difference is this use of varying particle sizes in the target model.

To further study the effect of different particle sizes, a set of calculations was run in which the size of the particles in the target differed from the size of the particles in the penetrator. For all these single-disk calculations, the penetrator had a constant smoothing length of 0.03175 cm, using one particle per smoothing length. For each calculation, the smoothing length of the target was varied, using one particle per smoothing length. Calculations were run in which the relative sizes of the target particles, with respect to the penetrator particles, were 0.50, 0.65, 0.80, 1.25, 1.30, and 2.00. These cases resulted in target smoothing lengths of 0.01588 cm, 0.02064 cm, 0.02540 cm, 0.03969 cm, 0.04128 cm, and 0.06350 cm, respectively.

The case in which the target particles are 1.30 times the size of the penetrator is special in that this configuration produces target and penetrator particles of nearly identical mass. The calculations were run to 40 μs, and the solutions were compared to the baseline case in which the target and penetrator had equal sized particles (a relative target particle size of 1.00).

Material plots at 40 μs for the cases using particle size ratios of 0.50, 1.00, 1.30, and 2.00 are shown in Figure 15. These plots show the dramatic effect of the variation of the particle size in the target relative to that in the penetrator. The material plot in Figure 15a shows the result for the case in which the penetrator particles are twice the size of the target particles. For this case and the others in which the ratio of target to penetrator particle size was less than unity, the disk penetrated much deeper into the target than the experiment. In fact, at 40 μs, the penetration is still not complete for these cases. Defining the penetrator particles to be larger than those in the target tends to make the penetrator more rigid and increases its ability to penetrate the target.

The material plot in Figure 15b shows the result of the baseline calculation in which the penetrator and the target were defined with identical particle sizes (ratio = 1.00). Figure 15c and 15d provide the material plots for two of the three cases in which the target particles were larger than those in the penetrator. For each calculation of this type (ratio > 1.00) the target material behaved in a more rigid manner than in the baseline case. The most extreme case was the one in which the target particles were twice the size of the penetrator particles. In this case, the penetrator leaves only a small indentation in the target and then bounces off the target and breaks into pieces.

These results help to explain the difference found between the convergence properties of the 2D and 3D solutions. It is possible that if the 3D calculations described earlier had been run with a constant particle size, instead of varying the particle size in the target, the 3D code may have produced greater final penetrations, bringing them in closer agreement with the 2D results and the experimental data. Further examination of the formulation of the SPH algorithm is required to determine the cause of the huge variations between these calculations.

7. VARIATION OF SMOOTHING LENGTH RETAINING CONSTANT PARTICLE SIZE

All the calculations described so far were set up to define particle sizes as being equal to the smoothing length. Put another way, each calculation used only one particle per smoothing length. It is not necessary, however, to set up problems in this manner. One possible variation on problem definition would be to increase both the smoothing length and the number of particles per smoothing length, thereby retaining the particle size and total number of particles in the simulation. Increasing the smoothing length would have two primary effects on the solution. First, the number of neighbors of a particular particle would increase, thereby increasing the number of particles used in updating the state variables at every time step. This would create more work to be done at every time step for each particle.

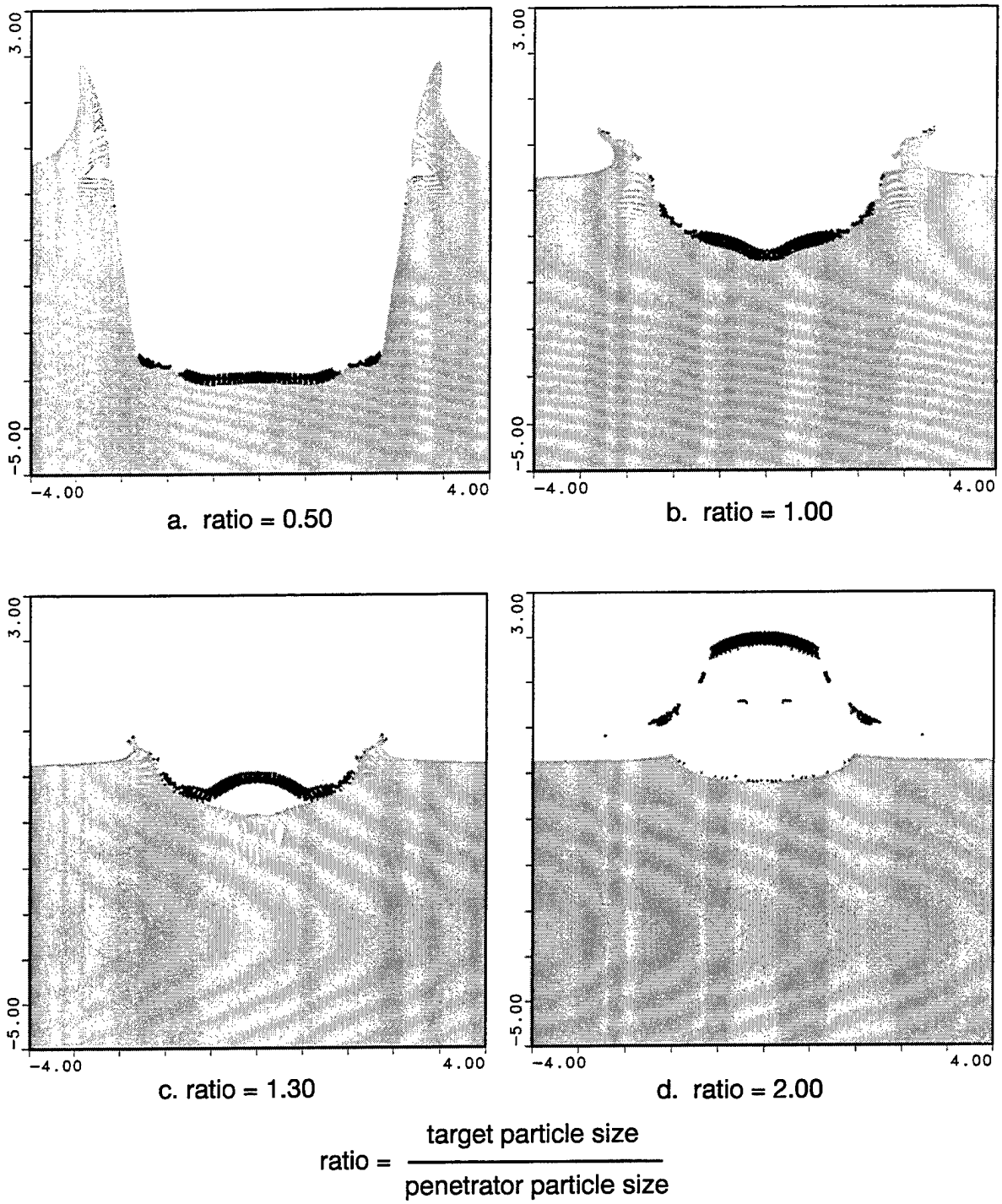

Figure 15. Single-disk impact at 40 μs for particle size ratios of: (a.) 0.50, (b.) 1.00, (c.) 1.30, and (d.) 2.00.

For 2D calculations, the number of neighboring particles used in updating the state variables is proportional to the square of the smoothing length, resulting in a workload increase that is proportional to h^2. Second, since the size of the time step is directly proportional to the smoothing length, the time step would increase, resulting in fewer iteration cycles required to complete the simulation, resulting in a decrease in workload that is proportional to h. Therefore, for a set of 2D calculations of this type, the time required to complete a simulation should be proportional to the smoothing length, h. Using this logic, it can be seen that the time required for a set of 3D calculations would be proportional to the square of the smoothing length.

A final set of axisymmetric calculations was performed by taking this approach to model the single-disk impact experiments. A constant particle size of 0.03175 was employed, resulting in a total of 99,625 particles in each calculation. Each calculation was run to a simulated time of 40 μs. As in the other calculations, Lagrangian tracer particles were used to gather position histories of the penetrator and target materials. The characteristics of these calculations and their resulting final penetration depths are provided in Table 4.

Table 4. Calculations in Smoothing Length Variation Study.

h (cm)	Number of Particles per h	Iteration Cycles	Computer Time (hours)	Penetration Depth (cm)
0.03175	1	2150	2.8	1.43
0.06350	2	1155	5.5	1.29
0.12700	4	581	11.0	1.21
0.25400	8	286	22.0	1.08
0.50800	16	160	50.7	0.60

Table 4 shows that the estimated workload associated with these calculations closely follows the expectation; the number of iteration cycles decreased in proportion to the increase in smoothing length, and the total computer time increased proportionally with the smoothing length. The most dramatic result of this set of calculations was the effect of smoothing length on the resulting simulation. Table 4 shows that as the smoothing length was increased, the penetration depth decreased significantly. This decrease in penetration depth initially suggests that the increase in smoothing length tends to artificially increase the rigidity of the materials and therefore inhibit penetration. Further examination of the results shows that the calculations differ not only in final penetration depth but in the basic characteristics of the impact event. Figure 16 shows the y-position (axial) histories of the tracer particle located at the center of the target for each of the calculations. The solid line presents the results of the baseline calculation using one particle per smoothing length. A detailed description of the penetration event for this calculation was provided earlier in this report. The figure shows that calculations employing more than one particle per smoothing length produced entirely different penetration histories from the baseline calculation. The final penetration depth produced by the baseline calculation is in closer agreement with the experimental data than those calculations using more than one particle per smoothing length. Furthermore, calculations with other grid-based codes produced results simular to

those created by the baseline calculation. These findings suggest that it is best to run Magi calculations of high velocity impact with one particle per smoothing length. Further study of the numerical formulation of the SPH method is necessary to determine the cause of the significant differences between these calculations.

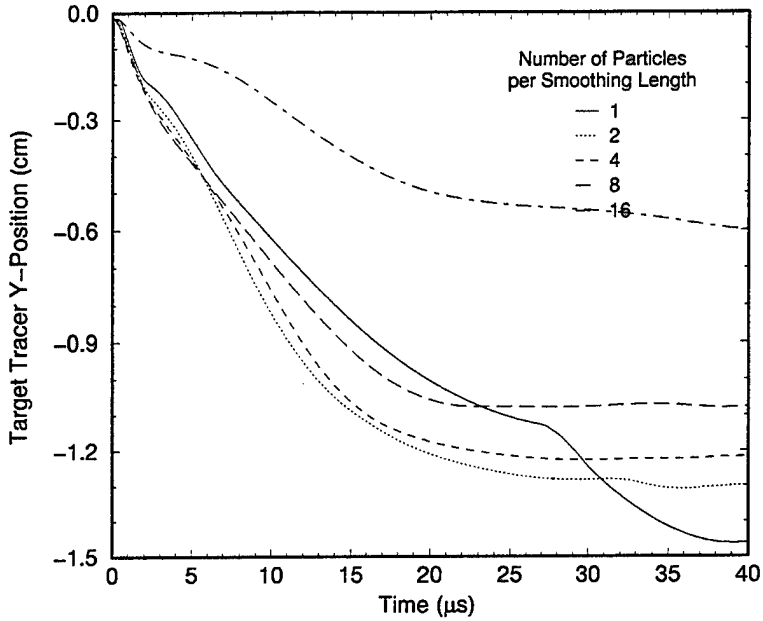

Figure 16. Penetration Histories from Smoothing Length Variation Study.

8. SUMMARY AND RECOMMENDATIONS

This report has documented the simulation of a set of disk-shaped penetrator impact experiments with the SPH code Magi. The 2D implementation of the code was tested extensively to reveal some of the strengths and weaknesses of the SPH method for simulating high velocity impact problems. Particle resolution studies were performed to determine the ability of the 2D and 3D implementations of the code to converge on a final penetration depth. These calculations revealed that approximately 10 particles are required across any critical dimension to properly capture the transient compression and expansion waves that occur during such impact events. In the case of the disk impact cases examined here, this critical dimension is the thickness of the penetrator. As the particle size was refined, the calculational results fell within the range of uncertainty of the experimental data for a single-disk impact event, 6.5% below the mean of the experimental mean penetration depth. Calculations were also performed for cases involving two and four axially aligned disk projectiles with penetration depths predicted to within 11.5% of experimental results.

Additional sets of calculations were performed to determine the effects of increasing the number of particles per smoothing length and the interaction of different sized particles.

These calculations produced results that differed drastically from the experimental data. Overall, the best results were obtained by using a contant particle size throughout the computational domain with one particle per smoothing length. The SPH method and specific Magi programming must be studied in greater detail to understand the possible causes of these problems.

Of course, these disk impact simulations alone are not sufficient to fully evaluate the viability of SPH in armor/anti-armor applications. However, they do provide a positive initial step in assessing the dominant computational characteristics of this method. Additional calculations, particulary in 3D, over a wide variety of configurations of interest are required to complete the evaluation. Experimental data exist for yawed, oblique long-rod penetrator impact, and the detonation/formation of an explosively formed projectile. Further investigation of SPH through its application to problems of this type is essential to formulating an accurate assessment of the technology.

INTENTIONALLY LEFT BLANK

REFERENCES

Backman, M.E. and W. Goldsmith. The Mechanics of Penetration of Projectiles into Targets. *International Journal of Engineering Science*, **16**, 1-99, (1978).

Belytschko, T. Nonlinear Analysis - Description and Stability, in: Structural Mechanics Computer Programs, Reviews and Summaries. Pilkey, W. and B. Pilkey, eds. Shock and Vibration Information Center, Washington DC, 1975.

Benson, D.J. Computational Methods in Lagrangian and Eulerian Hydrocodes. *Computer Methods in Applied Mechanics and Engineering*, **99**, 235-394 (1992).

Bjerke, T.W., J.A. Zukas, and K.D. Kimsey. Penetration Performance of Disk Shaped Penetrators. *International Journal of Impact Engineering*, **12**, 263-280 (1992).

Bjerke, T.W. Private Communication. 1997.

Blazynski, T.Z. Materials at High Strain Rates. Elsevier Applied Science, London and New York, 1987.

Brissenden, C. Performance of Novel KE Penetrator Designs Over the Velocity Range 1600 to 2000 m/s. Thirteenth International Symposium on Ballistics, Stockholm, Sweden, 183-190 (1992).

Charters, A.C. The Penetration of Rolled Homogeneous Armor by Continuous and Segmented Rods at High Velocity: Theory and Experiment. General Research Corporation Report CR-87-1008 (1987).

Charters, A.C., T.L. Menna, and A.J. Piekutowski. Penetration Dynamics of Rods from Direct Ballistic Tests of Advanced Armor Concepts at 2-3 km/s. *International Journal of Impact Engineering*, **10**, 93-106 (1990).

Charters, A.C., and D.L. Orphal. The Segmented Rod: A New Concept for the Defeat of Advanced Armor. *Journal of Defense Research* (1990).

Cline, C.F., R.P. Gogolewski, and J.E. Reaugh. Low Fineness Ration Kinetic Energy Projectiles. Eleventh International Symposium on Ballistics - Volume II, Brussels, Belgium, 277-283 (1989).

Cuadros, J.H. Monolithic and Segmented Projectile Penetration Experiments in the 2 to 4 Kilometers per Second Impact Regime. *International Journal of Impact Engineering*, **10**, 147-157 (1990).

De Rosset, W.S., and T.M. Sherrick. Segmented Rod Performance at Ordnance Velocity. U.S. Army Research Laboratory report ARL-MR-291, February 1996.

Frank, K., and J. Zook. Chunky Metal Penetrators Act Like Constant Mass Penetrators. Twelfth International Symposium on Ballistics - Volume I. San Antonio, TX, 441-449 (1990).

Goldsmith, W. Impact. Edward Arnold, London, 1960.

Hauver, G.E., and A. Melani. Behavior of Segmented Rods During Penetration. Ballistic Research Laboratory Technical Report BRL-TR-3129 (1990).

Herbette, G. The Influence of Projectile Shape on Penetration Power. Eleventh International Symposium on Ballistics - Volume II, Brussels, Belgium, 561-567 (1989).

Hermann, W. Nonlinear Transient Response of Solids, in: Structural Mechanics Computer Programs, Reviews and Summaries. Pilkey, W. and B. Pilkey, eds. Shock and Vibration Information Center, Washington DC, 1975.

Hohler, V., and A.J. Stilp. Penetration Performance of Segmented Rods at Different Spacing - Comparison with Homogeneous Rods at 2.5 - 3.5 km/s. Twelfth International Symposium on Ballistics - Volume III. San Antonio, TX, 178-187 (1990).

Holland, P.M., J.T. Gordon and A.C. Charters. Hydrocode Results for the Penetration of Continuous, Segmented, and Hybrid Rods Compared With Ballistic Experiments. *International Journal of Impact Engineering*, **10**, 241-250, (1990).

Hunkler, R. Numerical Simulation of Segmented Rods. Eleventh International Symposium on Ballistics, Brussels, Belgium (1989).

Johnson, W. Impact Strength of Materials. Crane, Russak, New York, 1972.

Kivity, Y., E. Yitzhak, and E. Hirsh. Penetration of Segmented Rods into Homogeneous Targets. Eleventh International Symposium on Ballistics - Volume II, Brussels, Belgium, 473-480 (1989).

Libersky, L.D., A.G. Petschek, T.C. Carney, J.R. Hipp, and F.A. Alladadi. High Strain Rate Lagrangian Hydrodynamics: A Three-Dimensional SPH Code for Dynamics Material Response. *Journal of Computational Physics*, Vol. 109, No. 1 (1993).

Mescall, F.J. Shock Wave Propagation in Solids, in: Structural Mechanics Computer Programs. Pilkey, W., S. Saczalski and H. Schaffer, eds. University of Virginia Press, Charlottesville, VA, 1974.

Naz, P., and H.F. Lehr. The Crater Formation Due to Segmented Rod Penetrators. *International Journal of Impact Engineering*, **10**, 413-425, (1990).

Orphal, D.L., C.E. Anderson, and R.R. Franzen. Impact Calculations of $L/D \leq 1$ Penetrator. Twelfth International Symposium on Ballistics, San Antonio, TX, 458-464 (1990)

Orphal, D.L., and R.R. Franzen. Penetration Mechanics and Performance of Segmented Rods Against Metal Targets. *International Journal of Impact Engineering*, **10**, 427-438, (1990).

Orphal, D.L., C.E. Anderson, R.R. Franzen, J.D. Walker, and P.N. Schneidewind. Penetration by $L/D \leq 1$ Projectiles. Thirteenth International Symposium on Ballistics, Volume 3, Stockholm, Sweden, 235-242 (1992).

Randles, P.W. and L.D. Libersky. Smoothed Particle Hydrodynamics: Some Recent Improvements and Applications. *Computer Methods in Applied Mechanics and Engineering*, (1996).

Raatschen, H.J., W. Pavel, S. Fuchs, H. Senf, and H. Rothenhausler. Penetration Efficiency of Segmented Rods. Eleventh International Symposium on Ballistics - Volume II, Brussels, Belgium, 493-500 (1989).

Scheffler D.R. 2D Comuter Simulations of Segmented Penetrators Impacting Semi-Infinite Steel Targets. *International Journal of Impact Engineering*, **9**, 35-43, (1990).

Scheffler D.R., and J.A. Zukas. Numerical Simulation of Segmented Penetrator Impact. *International Journal of Impact Engineering*, **10**, 487-498, (1990).

Sorensen, B.R., K.D. Kimsey, G.F. Silsby, D.R. Scheffler, T.M. Sherrick, and W.S. De Rosset. High Velocity Penetration of Steel Targets. *International Journal of Impact Engineering*, **11**, 107-119, (1991).

Tate, A. Engineering Modelling of Some Aspects of Segmented Rod Penetration. *International Journal of Impact Engineering*, **9**, 327-341, (1990).

Von Rieseman, W.A., J.A. Stricklin and W.E. Haisler. Nonlinear Continuua, in: Structural Mechanics Computer Programs. Pilkey, W., S. Saczalski and H. Schaffer, eds. University of Virginia Press, Charlottesville, VA, 1974.

Zukas, J.A. Numerical Simulation of Semi-Infinite Target Penetration by Continuous and Segmented Rods. Ballistic Research Laboratory Technical Report BRL-TR-3081 (1990).

Zukas, J.A., Editor. Impact Dynamics. Wiley-Interscience, New York, 1982.

Zukas, J.A., T. Nicholas, H.F. Swift, L.B. Greszczuk, and D.R. Curran. High Velocity Impact Dynamics. Wiley-Interscience, New York, 1990.

INTENTIONALLY LEFT BLANK

NO. OF COPIES	ORGANIZATION
2	ADMINISTRATOR DEFENSE TECHNICAL INFO CENTER ATTN DTIC DDA 8725 JOHN J KINGMAN RD STE 0944 FT BELVOIR VA 22060-6218
1	DIRECTOR US ARMY RESEARCH LABORATORY ATTN AMSRL CS AL TA REC MGMT 2800 POWDER MILL RD ADELPHI MD 20783-1197
1	DIRECTOR US ARMY RESEARCH LABORATORY ATTN AMSRL CI LL TECH LIB 2800 POWDER MILL RD ADELPHI MD 207830-1197
1	DIRECTOR US ARMY RESEARCH LABORATORY ATTN AMSRL CS AL TP TECH PUB BR 2800 POWDER MILL RD ADELPHI MD 20783-1197
1	HQDA DAMO DENNIS SCHMIDT 400 ARMY PENTAGON WASHINGTON DC 20310-0460
1	OSD OUSD (A&T) /ODDDR&E(R) ATTN J LUPO THE PENTAGON WASHINGTON DC 20310-7100
1	CECOM SP & TERRESTRIAL COM DIV ATTN AMSEL RD ST MC M H SOICHER FT MONMOUTH NJ 07703-5203
1	CECOM PM GPS COL S YOUNG FT MONMOUTH NJ 07703
1	GPS JOINT PROG OFC DIR COL J CLAY 2435 VELA WAY STE 1613 LOS ANGELES AFB CA 90245-5500
1	ELECTRONIC SYSTEMS DIV DIR CECOM RDEC J NIEMELA FT MONMOUTH NJ 07703

NO. OF COPIES	ORGANIZATION
3	DARPA L STOTTS J PENNELLA B KASPAR 3701 N FAIRFAX DR ARLINGTON VA 22203-1714
1	US MILITARY ACADEMY MATHEMATICAL SCIENCES CENTER OF EXCELLENCE DEPT OF MATHEMATICAL SCIENCES ATTN MDN A MAJ DON ENGEN THAYER HALL WEST POINT NY 10996-1786
6	COMMANDER US ARMY ARDEC ATTN AMSTA AR AEE WW E BAKER C CHIN R FONG J PEARSON J WALSH TECH LIB PICATINNY ARSENAL NJ 07806-5000
1	COMMANDER US ARMY ARDEC ATTN AMSTA AR AET M TECH LIBRARY PICATINNY ARSENAL NJ 07806-5000
1	COMMANDER US ARMY ARDEC ATTN AMSTA AR FS E ANDRICOPOULOS PICATINNY ARSENAL NJ 07806-5000
3	CDR US ARMY MERDEC ATTN AMSME RD ST WF L CRAFT D LOVELACE M SCHEXNAYDER REDSTONE ARSENAL AL 35898-5250
1	DIR US ARO WASH ATTN AMXRO W KA BANNISTER ROOM 8N31 5001 EISENHOWER AVE ALEXANDRIA VA 22333-0001
3	COMMANDER US ARMY RESEARCH OFFICE ATTN J CHANDRA K IYER TECH LIB PO BOX 12211 RESEARCH TRIANGLE PARK NC 27709-2211

NO. OF COPIES	ORGANIZATION
4	COMMANDER US ARMY CORPS OF ENGINEERS ATTN J BALSARA T BLEVINS P PAPIDOS R NAMBURU 3909 HALL FERRY ROAD VICKSBURG MS 39180-6199
3	DARPA ATTN J RICHARDSON B WILCOX TECH LIBRARY 3701 N FAIRFAX DR ARLINGTON VA 22203-1714
2	CDR US ARMY TACOM ATTN AMSTA RSK J THOMPSON S GOODMAN WARREN MI 48397-5000
2	DIR NRL ATTN J A NEMES A E WILLIAMS CODE 6684 4555 OVERLOOK AVE SW WASHINGTON DC 20375
2	CDR NSWC ATTN W H HOLT W MOCK CODE G22 17320 DAHLGREN ROAD DAHLGREN VA 22448-5000
8	CDR NSWC ATTN C S COFFEY R K GARRETT JR H MAIR R12 J MCKIRGAN B PARK D G TASKER TECH LIB F ZERILLI 10901 NEW HAMPSHIRE AVENUE SILVER SPRING MD 20903-5000
2	COMMANDER NWC ATTN T GILL CODE 3261 TECHNICAL LIBRARY CHINA LAKE CA 93555-6001
1	NAVAL POST GRAD SCHOOL ATTN J STERNBERG CODE 73 MONTEREY CA 93943
1	USAF PHILLIPS LAB ATTN PL WSCD F ALLAHDADI KIRTLAND AFB NM 87185
1	USAF WAL ATTN T NICHOLAS WRIGHT-PATTERSON AFB OH 45433

NO. OF COPIES	ORGANIZATION
4	USAF WL ATTN MNMW W COOK J FOSTER M NIXON TECH LIB EGLIN AFB FL 32542-5434
2	COMMANDER FC DSWA ATTN FCTTS E MARTINEZ P RANDLES KIRTLAND AFB NM 87115
11	DIR LOS ALAMOS NATL LAB ATTN J BOLSTAD CIC-ACL T CARNEY EES-5 MS C305 E FERM DX-3 MS P940 G T GRAY MST-8 MS G755 K HOLIAN CIC-12 MS D413 L HULL DX-3 MS P940 J JOHNSON F663 L LIBERSKY X-HM MS D413 D A MANDELL X-CI MS F663 L SCHWALBE X-HM MS D413 TECH LIBRARY PO BOX 1663 LOS ALAMOS NM 87545
11	DIR LAWRENCE LIVERMORE NATL LAB ATTN R COUCH L170 M FINGER L159 W H GOURDIN L355 G GOUDREAU L125 C HOOVER L125 D LASSILA L170 P RABOIN L125 J E REAUGH L282 M J MURPHY L282 TECH LIB R E TIPTON L170 PO BOX 1663 LIVERMORE CA 94550
2	DIR SANDIA NATL LABORATORIES ATTN D BAMMANN MS 9405 M CHIESA MS 9042 PO BOX 969 LIVERMORE CA 94550
12	DIR SANDIA NATL LABORATORIES ATTN R M BRANNON MS 0820 D E CARROL MS 0819 L C CHABILDAS MS 1181 M FORRESTAL MS 0315 E S HERTEL JR MS 0819 M KIPP MS 0820 J M MCCLAUN MS 1202 J S PEERY MS 0819 S A SILLING MS 0820 R M SUMMERS MS 0819 T TRUCANO MS 0819 P YARRINGTON MS 0820 PO BOX 5800 ALBUQUERQUE NM 87185-0307

NO. OF COPIES	ORGANIZATION
1	AEROJET ELECTRO SYS CO ATTN WARHEAD SYSTEMS J CARLEONE PO BOX 296 AZUSA CA 91702
4	ALLIANT TECHSYSTEMS INC ATTN S BEISSEL R STRYK T HOLMQUIST MN11 2720 G R JOHNSON MN11 2925 7225 NORTHLAND DRIVE BROOKLYN PARK MN 55428
1	ALME AND ASSOC ATTN M L ALME 102 STEVENS FOREST PROF 9650 SANTIAGO ROAD COLUMBIA MD 21045
1	APPLIED RESEARCH ASSOCIATES INC ATTN J D YATTEAU 5941 S MIDDLEFIELD RD STE 100 LITTLETON CO 80123
2	APPLIED RESEARCH ASSOCIATES INC ATTN J KEEFER N ETHRIDGE PO BOX 548 ABERDEEN MD 21001
4	APPLIED RESEARCH ASSOCIATES INC ATTN J CREPEAU S HIKIDA C NEEDHAM R NEWELL 4300 SAN MATEO BLVD STE A220 ALBUQUERQUE NM 87110
1	BRIGS CO ATTN J E BACKOFEN 2668 PETERSBOUGH ST HERNDON VA 22071-2443
1	COMPUTATIONAL MECH ASSN ATTN J A ZUKAS PO BOX 11314 BALTIMORE MD 21239-0314
3	DYNA EAST CORP ATTN P C CHOU R CICCARELLI W FLIS 3620 HORIZON DRIVE KING OF PRUSSIA PA 19406

NO. OF COPIES	ORGANIZATION
2	GEN RSCH CORP ATTN A CHARTERS T MENNA 5383 HOLLISTER AVE SANTA BARBARA CA 93111
1	IAT UNIV OF TEXAS AT AUSTIN PO BOX 202797 AUSTIN TX 78720-2797
5	IAT UNIV OF TEXAS AT AUSTIN ATTN S J BLESS H D FAIR T M KIEHNE D LITTLEFIELD M J NORMANDIA 4030 2 W BRAKER LN AUSTIN TX 78759-5329
1	IRA INC ATTN D ORPHAL 4450 BLACK AVE STE E PLEASANTON CA 94566
1	KAMAN SCIENCES CORP ATTN J S WILBECK 7600 BLVD S STE 208 HUNTSVILLE AL 35802
1	KAMAN SCIENCES CORPORATION ATTN N ARI PO BOX 7463 COLORADO SPRINGS CO 80933-7463
1	D R KENNEDY & ASSOC INC ATTN D KENNEDY PO BOX 4003 MOUNTAIN VIEW CA 94040
1	KERLEY PUB SVC ATTN G I KERLEY PO BOX 13835 ALBUQUERQUE NM 87192-3835
3	LIVERMORE SOFTWARE TECH CORP ATTN J O HALLQUIST B MAKER D STILLMAN 2876 WAVERLY WAY LIVERMORE CA 94550
1	LOGICON RDA ATTN B LEE 6053 W CENTURY BLVD LOS ANGELES CA 90045

NO. OF COPIES	ORGANIZATION
1	ORLANDO TECH INC ATTN D A MATUSKA PO BOX 855 SHALIMAR FL 32579
3	S CUBED ATTN J BARTHEL S ROGERS R SEDGWICK PO BOX 1620 LA JOLLA CA 92037-1620
3	SOUTHWEST RESEARCH INSTITUTE ATTN C ANDERSON S MULLIN J WALKER 8500 CULEBRA ROAD PO DRAWER 28510 SAN ANTONIO TX 78284
2	SRI INTERNATIONAL ATTN D CURRAN L SEAMAN 333 RAVENWOOD AVENUE MENLO PARK CA 94025
1	ZERNOW TECH SVC INC ATTN L ZERNOW 425 W BONITA AVE STE 208 SAN DIMAS CA 91773
	ABSTRACT ONLY
1	PRIN DPTY FOR TECH GY HDQ US ARMY MATL CMND ATTN AMCDCG T M FISETTE 5001 EISENHOWER AVE ALEXANDRIA VA 22333-0001
1	PRIN DPTY FOR ACQTN HDQ US ARMY MATL CMND ATTN AMCDCG A D ADAMS 5001 EISENHOWER AVE ALEXANDRIA VA 22333-0001
1	DPTY CG FOR RDE HDQ US ARMY MATL CMND ATTN AMCRD BG BEAUCHAMP 5001 EISENHOWER AVE ALEXANDRIA VA 22333-0001
	ABERDEEN PROVING GROUND
2	DIRECTOR US ARMY RESEARCH LABORATORY ATTN AMSRL CI LP (TECH LIB) BLDG 305 APG AA

NO. OF COPIES	ORGANIZATION
38	DIR US ARMY RSCH LABORATORY ATTN AMSRL WM T W MORRISON AMSRL WM TA W BRUCHEY JR J DEHN G FILBEY JR W GILLICH W GOOCH JR Y HAUNG D KLEPONIS H MEYER JR A MIHALCIN E RAPACKI JR AMSRL WM TB R FREY J STARKENBERG R LOTTERO AMSRL WM TC T BJERKE R COATES W DE ROSSET F GRACE K KIMSEY M LAMPSON L MAGNESS D SCHEFFLER S SCHRAML (5 CYS) W WALTERS AMSRL WM TD R L BITTING A M DIETRICH JR T FARRAND K FRANK N GNIAZDOWSKI F GREGORY D J GROVE P KINGMAN M RAFTENBERG A RAJENDRAN M SCHEIDLER S SCHOENFELD S SEGLETES T W WRIGHT

REPORT DOCUMENTATION PAGE

Form Approved
OMB No. 0704-0188

Public reporting burden for this collection of information is estimated to average 1 hour per response, including the time for reviewing instructions, searching existing data sources, gathering and maintaining the data needed, and completing and reviewing the collection of information. Send comments regarding this burden estimate or any other aspect of this collection of information, including suggestions for reducing this burden, to Washington Headquarters Services, Directorate for Information Operations and Reports, 1215 Jefferson Davis Highway, Suite 1204, Arlington, VA 22202-4302, and to the Office of Management and Budget, Paperwork Reduction Project (0704-0188), Washington, DC 20503.

1. AGENCY USE ONLY *(Leave blank)*	2. REPORT DATE	3. REPORT TYPE AND DATES COVERED
	August 1998	Final

4. TITLE AND SUBTITLE

Smoothed Particle Hydrodynamics Simulation of Disk-Shaped Penetrator Impact

5. FUNDING NUMBERS

PR: 61102AH43

6. AUTHOR(S)

Schraml, S.J.; Kimsey, K.D. (both of ARL)

7. PERFORMING ORGANIZATION NAME(S) AND ADDRESS(ES)

U.S. Army Research Laboratory
Weapons & Materials Research Directorate
Aberdeen Proving Ground, MD 21010-5066

8. PERFORMING ORGANIZATION REPORT NUMBER

9. SPONSORING/MONITORING AGENCY NAME(S) AND ADDRESS(ES)

U.S. Army Research Laboratory
Weapons & Materials Research Directorate
Aberdeen Proving Ground, MD 21010-5066

10. SPONSORING/MONITORING AGENCY REPORT NUMBER

ARL-TR-1766

11. SUPPLEMENTARY NOTES

12a. DISTRIBUTION/AVAILABILITY STATEMENT

Approved for public release; distribution is unlimited.

12b. DISTRIBUTION CODE

13. ABSTRACT *(Maximum 200 words)*

Smoothed particle hydrodynamics (SPH) is a method of continuum mechanics analysis in which materials are modeled by a discrete set of particles. The SPH code Magi has been used to simulate the penetration of a semi-infinite steel target by tungsten alloy disks traveling at an initial impact velocity of 2 km/s. Calculations wee performed to simulate experimental configurations using one, two, and four disks. All disks had a constant length-to-diameter ratio of 0.125. The computed penetration depth into the target material is compared to the experimental data for each case. The study included a set of calculations in which the problem resolution was varied to determine the ability of the method to converge on a penetration depth as the number of particles in the problem was increased. Advantages and limitations observed in the application of SPH to the field of penetration mechanics are discussed.

14. SUBJECT TERMS

impact
numerical simulation
particle
penetrator

15. NUMBER OF PAGES

50

16. PRICE CODE

17. SECURITY CLASSIFICATION OF REPORT	18. SECURITY CLASSIFICATION OF THIS PAGE	19. SECURITY CLASSIFICATION OF ABSTRACT	20. LIMITATION OF ABSTRACT
Unclassified	Unclassified	Unclassified	